Aalto University
School of Electrical Engineering
Department of Electrical Engineering and Automation

Simo Vuorsalo

Realization of a Direct Soft Switching AC/AC Converter for Wireless Power Transfer Applications

School of Electrical Engineering

Thesis submitted for examination for the degree of
Master of Science in Technology.
Espoo 13.11.2015

Thesis Supervisor: Professor Jorma Kyyrä

Thesis Advisor: M.Sc. Ferdi Kusumah

Aalto University
School of Electrical Engineering
Department of Electrical Engineering and Automation

Aalto University
School of Electrical
Engineering

ABSTRACT OF THE MASTER'S THESIS

School of Electrical Engineering

Master's Programme in Electronics and Electrical Engineering

Author: Simo Vuorsalo

Title: Realization of a Direct Soft Switching AC/AC Converter for Wireless Power Transfer Applications

Date: 13.11.2015 | **Language:** English | **Number of pages:** 95

Professorship: Power Electronics | **Code:** S-81

Supervisor: Professor Jorma Kyyrä

Advisor: M.Sc. Ferdi Kusumah

This thesis describes the design, realization and testing of a three-phase to one-phase direct AC/AC converter, also known as the matrix converter. The switching is using the soft-switching strategy which is also known in the literature as the Zero Current Switching strategy. To achieve ZCS, the circuit needs resonant behavior which is achieved by the transmitter primary side that is an LC circuit. This circuit acts as a tank circuit and the switching frequency is the resonant frequency of the LC circuit. The design of the converter was done with OrCAD capture, PSPICE and Layout. The proposed converter was designed completely during the project as well as the printed circuit boards. The wireless power transfer is achieved by using an air-cored coil pair. The receiver circuit analysis is not in the scope of this thesis.

The testing of the converter was not able to perform completely while the complexity of the software prevented the project to be finished in given schedule. The partial test results are shown in the thesis.

Keywords: Direct converter, Matrix converter, ZCS, Soft switching, Wireless power transfer

Aalto University
School of Electrical Engineering
Department of Electrical Engineering and Automation

DIPLOMITYÖN TIIVISTELMÄ

Sähkötekniikan korkeakoulu

Elektroniikan ja sähkötekniikan koulutusohjelma

Tekijä: Simo Vuorsalo

Työn nimi: Suoran AC/AC-muuttajan suunnittelu langattomiin tehonsiirtosovelluksiin

Päiväys: 13.11.2015	**Kieli:** Englanti	**Sivumäärä:** 95

Professuuri: Tehoelektroniikka	**Koodi:** S-81

Valvoja: Professori Jorma Kyyrä

Ohjaaja: DI Ferdi Kusumah

Tämä diplomityö käsittää suoran AC-AC –muuttajan toteutuksen, suunnittelun ja testauksen. Muuttaja muuntaa kolmivaihesyötön yksivaiheiseen lähtöön. Kyseessä on matriisimuuttajan eräs sovellus. Kytkentä toimii ns. pehmeällä kytkennällä, eli kytkentähetkellä kytkimien virta on nollassa. Tämä saavutetaan kun kuormana toimii kelan ja kondensaattorin sarjaankytkentä, jonka virta toimii myös takaisinkytkentänä kytkinten ohjaukselle. Muuttajan langattoman tehonsiirron osuus toteutettiin käytännössä ilmasydämisellä kelalla. Toteutus tehtiin tässä projektissa vain ensiöpuolelle. Toisiopuolta ei tässä työssä käsitellä.

Suunnittelu toteutettiin OrCAD-ohjelmistolla. Suunnittelun kannalta oleelliset piirit simuloitiin OrCAD PSPICE:llä. Lisäksi työssä esitetään komponenttiarvojen laskenta. Toteutettu laite tehtiin osana projektia, jolloin laitetta varten tehtiin myös piirilevyt.

Muuttajan testausta ei ehditty tekemään loppuun annetussa aikamäärässä valmiiksi. Syynä tähän oli hilaohjauksen monimutkaisuus, joka venytti ohjelmiston kehittämistä. Osittainen testaus on esitetty työssä.

Avainsanat: suora muuttaja, matriisimuuttaja, langaton tehonsiirto

Acknowledgments

I want to thank my advisor MS.c. Ferdi Kusumah who helped me significantly in order to finish this thesis. Also, I want to thank Prof. Jorma Kyyrä for giving the opportunity to join this incredibly interesting research project, and of course, all the help given during the project. The feedback was valuable when the thesis was in progress.

I want to thank my former colleagues and co-students Marko Häkkinen and Konsta Ruotsalainen, whom without I probably couldn't have been able to finish my studies. I wish them all the best during their final studies in Aalto University.

Espoo 13.11.2015

Simo Vuorsalo

Table of Contents

Abbreviations

AC	Alternating current
ADC	Analog-to-Digital Converter
CE	Conformité Européenne
DC	Direct Current
EMI	Electromagnetic Interference
ESR	Equivalent Series Resistance
EV	Electric Vehicle
FOM	Figure of Merit
HEV	Hybrid Electric Vehicle
IC	Integrated Circuit
IGBT	Insulated Gate Bipolar Transistor
MC	Matrix Converter
MCU	Microcontroller Unit
OLEV	On-Line Electric Vehicle
PCB	Printed Circuit Board
RF	Radio Frequency
SiC MOSFET	Silicon Carbide MOSFET
TIM	Thermal Interface Material
V2G	Vehicle-to-Grid
WPT	Wireless Power Transfer
VTR	Voltage Transfer Ratio
ZCS	Zero Current Switching

ZVS	Zero Voltage Switching

Symbols

a, b	Measures of an inductor, see Figure 13
A_{WIRE}	Area of the litz wire
C	Capacitance
C_i	Capacitance for primary and secondary. i = 1 for primary, i = 2 for secondary
C_P	Primary Capacitance
d_0	Litz wire diameter with insulation
d_l	Litz wire diameter without insulation
d_{lopt}	Optimum strand diameter of the litz wire
E_{DRR}	Diode reverse recovery energy of the soft switching IGBT
E_{IOFF}	Turn-off energy of the soft switching IGBT
E_{ION}	Turn-on energy of the soft switching IGBT
E_{OFF}	Turn-off energy of an IGBT
E_{ON}	Turn-on energy of an IGBT
E_{REC}	Reverse recovery energy of an IGBT
f_0	Resonant Frequency
F_R	AC/DC resistance
f_{RES}	Resonant Frequency of the RLC circuit
f_{SW}	Switching Frequency
I	Current
i	i = 1 for primary, i = 2 for secondary
I_n	Capacitor Current at n^{th} frequency component

ΔI_{C}	Collector current change
ΔI_{D}	Current change in an IGBT diode
k	Coupling Factor
$\mathrm{k_{litz}}$	Number of wire strands of a litz wire
L_{i}	Inductance for primary and secondary. i = 1 for primary, i = 2 for secondary
L_{P}	Primary Inductance
L_{S}	Secondary Inductance
M	Mutual Inductance
$\mathrm{N_l}$	Number of wire bundles of a litz wire
$\mathrm{N_{ll}}$	Effective number of wire layers in a litz wire
P_{CI}	Power loss of an IGBT during conduction
P_{GATE}	Gate Driver Power loss
P_{H}	Capacitor power loss
P_{I}	Total power loss of an IGBT
P_{LOSS}	Average power loss in W_{Li}
P_{SWD}	Power loss of an IGBT diode during switching
P_{SWI}	Power loss of an IGBT during switching
Q	Quality Factor
Q_{i}	Quality Factor of the Inductor
R	Resistance
r_{c}	Collector to emitter dynamic resistance
r_{d}	Dynamic resistance of an IGBT diode
R_{eq}	Equivalent Resistance of the WPT system secondary

R_{i}	Parasitic resistance in series with L_{i},
R_n	Capacitor parasitic resistance at n$^{\mathrm{th}}$ frequency component
R_{thJA}	Junction-to-Air thermal resistance
R_{thJC}	Junction-to-Case thermal resistance
R_{thSA}	Heatsink-to-Air thermal resistance
R_{wDC}	DC resistance of the litz wire
$S_{\mathrm{a}}, S_{\mathrm{b}}, S_{\mathrm{c}}$	Switches for phases a, b and c
S_{jk}	Switching Function, $j \in \{a, b, c\}$, and $K \in \{A, B, C\}$
t	Time
T_{A}	Ambient Temperature
T_{D}	Internal temperature
t_{off}	Off-time of the duty cycle
t_{on}	On-time of the duty cycle
$tan\delta_{\mathrm{n}}$	Capacitor dissipation factor
V	Voltage
$\Delta V_{\mathrm{CE}}, \Delta V_{\mathrm{CE0}}$	Collector to emitter voltage derivatives
$\Delta V_{\mathrm{D}}, \Delta V_{\mathrm{D0}}$	Diode voltage derivatives
$V_{\mathrm{IN,VT}}$	Voltage transducer scaling circuit operational amplifier input voltage
$V_{\mathrm{OUT,VT}}$	Voltage transducer scaling circuit operational amplifier output voltage
W_{Li}	Peak inductor energy stored in inductor
Z	Impedance
γ_{SSOPT}	Load matching factor of the WPT coils

δ_W, δ	Skin depth of the litz wire, skin depth in general
η_{ff}	Maximum porosity factor of the litz wire
η_{max}	Maximum power transfer efficiency of the WPT system
μ_0, μ_r, μ	Permeabilities: Vacuum, Relative, product of vacuum and relative permeability
ρ_{Cu}	Copper resistivity
$\omega, \omega_0, \omega_n$	Angular Frequency, Angular Frequency at Resonant Frequency,

1 Introduction

In this thesis, a realization of a direct AC/AC converter is performed. Modified matrix converter topology is used to obtain wireless power transfer. The ultimate goal for the project is to achieve bi-directional power flow for the electric vehicle charger to be used either in a standalone charger or V2G solutions. This thesis is a part of a research project done concurrently and much of the background information is provided from the doctorate research of M.Sc. Ferdi Kusumah who is also an advisor for this thesis.

Direct AC/AC converters have been out for a while and the idea has been tested to be working in practical solutions, such as Yaskawa Varispeed AC series. The idea is to remove the bulky components from the conversion and achieve higher efficiency while achieving better power density. The converter is conversing the input AC voltage directly to AC output voltage without having DC bus stage in the converter. The huge downside is that the voltage transfer ratio is usually less than unity which makes it unappealing to motor drive solutions. Although matrix converter has this downside, it could have various other uses in many applications. These could be wireless power transfer, wind turbines, Vehicle-to-Grid, induction stoves and many more. However, having a downside of less than unity voltage transfer ratio, it still possesses a feature that is usable in many applications. This is because the matrix converters are usually bi-directional by their nature. The switches that are used in the switch matrix of the MC, are designed in such manner that they can deliver power in both directions. The power factor is generally very close to unity due to the sinusoidal current that is drawn from the mains network. This is a feature of the matrix converter that is superior to the other AC/AC converter topologies. The next sub-section describes the wireless power transfer in more detail and the last sub-section describes the thesis structure and gives the reader a brief description of each chapters.

1.1 Wireless Power Transfer

The idea of the wireless power transfer was first presented by Nikola Tesla in his apparatus for transmitting electrical energy (Tesla 1914). Much has happened since then and there are many projects globally researching the wireless power transfer for mobile phone chargers and automotive applications (WiTricity 2015). Magnetic resonance between a pair of magnetically coupled coil resonators are shown to be the best for efficient wireless power transfer. This has been also the focal point of the research (Hui,

Wenxing & Lee 2014). Figure 1 presents the equivalent circuit of the magnetically coupled circuit.

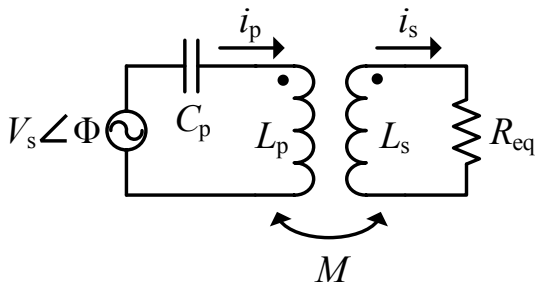

Figure 1: Equivalent circuit of a magnetically coupled circuit (Kusumah, Vuorsalo & Kyyrä 2015).

The mutual M inductance of the circuit can be obtained using Equation

$$\mathbf{M = k * \sqrt{L_P L_S}} \qquad (1\text{-}1)$$

, where

- k is the coupling factor,
- L_P is the primary side self-inductance
- L_S is the secondary side self-inductance.
- R_{eq} is the equivalent resistance
- C_P is the Primary side capacitance

After obtaining the mutual inductance, the voltages and currents can be evaluated by common circuit analysis methods using steady-state analysis. (Kusumah, Vuorsalo & Kyyrä 2015)

One team of researchers in KAIST has been developing a WPT system for buses which has the idea of integrating the transmitter circuit along the bus route. The bus then receives the power to its receiver devices and charges the batteries. This enables the bus to carry less batteries which can be considered as a positive side for overall efficiency of the system. The system is called On Line Electric Vehicle or OLEV. The measured efficiency is 80.81 % in a laboratory environment (Jaegue et al. 2013).

There has been plans to use wireless power transfer as a secondary back-up power source to transfer energy from the car batteries to home in emergency situations. Nissan has been developing such system (Nissan 2011).

1.2 Thesis in Brief

This thesis consists of seven chapters and the chapters are briefly introduced in the following description:

Chapter 1 is an introduction to the topic. It introduces the project briefly and let the reader to familiarize with the subject and discusses briefly about the wireless power transfer.

Chapter 2 discusses the non-trivial technological topics that were used in building and designing the converter.

Chapter 3 describes the actual design of the converter, such as component dimensioning and mathematical Equations.

Chapter 4 describes the actual realization and presents the practical results of the design phase.

Chapter 5 describes the testing of the converter and the comparison between the theoretical background and the experimental results.

Chapter 6 discusses the conclusions and findings of the prototype.

Chapter 7 is the final chapter and discusses the future of the application and the uses for the converter.

2 Direct converters and components

This chapter explains the basic operation of the matrix converter. The chapter explains the classification of the AC/AC converters. The matrix converter is generally an AC/AC converter without a bulky DC-link capacitor in the DC bus which the conventional AC/DC/AC converter uses. The converter to be designed in this thesis is discussed after presentation of the matrix converters. Finally, the future switching components are discussed.

2.1 Matrix Converter

The matrix converter (MC) is an AC/AC power converter based on semiconductor switches with minimal requirements for passive components. The switches are arranged in such manner, that any input phase can be connected to any output phase and the DC-link capacitor is not required. The name matrix derives from the fact that the switches are forming a matrix-like structure. Usually, there are nine switches, but the amount varies depending on the MC topology, number of input phases and the number of the output phases. The matrix converter first appeared in the literature in a book by Gyugi and Pelly in 1976 and a journal publication by Daniels and Slattery in 1978. It was also described as a “force commutated cycloconverter”. (Empiringham et al. 2013).

Although, some sources are claiming that the first study of MCs was presented in 1980 by Marco Venturini and Alberto Alesina. The main disadvantage of the MC is less than unity voltage transfer ratio (VTR) in majority of the topologies and control strategies. The first control strategy by Venturini and Alesina resulted as a VTR of 0.5 and later Venturini and Alesina improved their control method which resulted as a VTR of 0.866. This was called the optimum Venturini method or improved Venturini. (Szczesniak 2013)

There are also methods to increase the voltage transfer ratio in the MCs without DC energy storage. Ziogas et al increased VTR to 1.05 by using the indirect transfer function method. The work was done in 1986 for forced commutated cycloconverters (FCC) and the power factor is also controllable. The disadvantage of this method is that there is low frequency distortion in the output voltages and source currents. (Ziogas, Khan & Rashid 1986) The work of Casadei et al. shows that by using their proposal of SVM technique, one may achieve the VTR of 1.155. (Casadei et al. 2002). In the book (Szczesniak 2013), they showed that the matrix-reactance frequency converters can also reach VTR of over 1 but it requires additional switches due to the added chopper circuit.

Hybrid MCs can also reach VTR of over unity but they have small DC energy storages in the switch blocks of the converter. (Szczesniak 2013)

There are large amount of different matrix converter types and most of them are presented in the references (Kolar et al. 2011) and (Szczesniak 2013).

Basic Matrix converter circuit is shown in Figure 2.

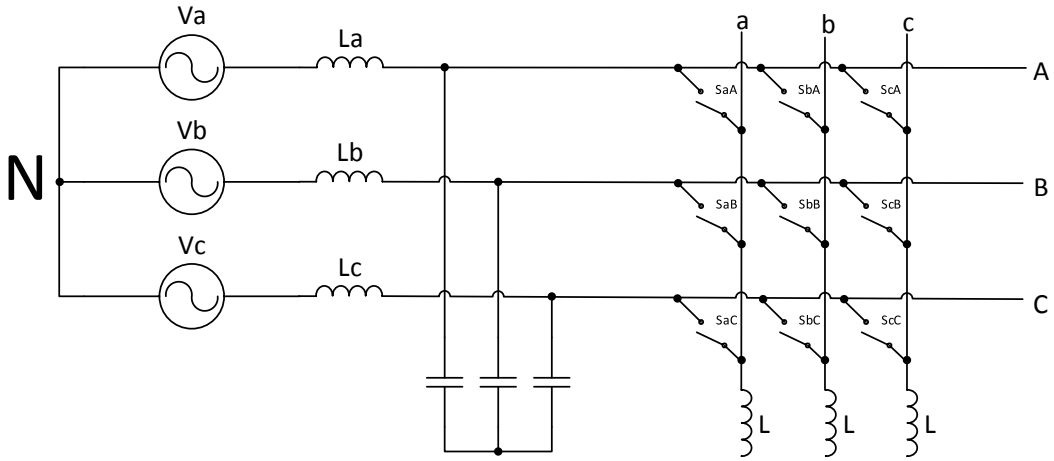

Figure 2: Simplified three-phase matrix converter (Szczesniak 2013).

The basic switching function is defined as shown in

$$S_{jK} = \begin{cases} \mathbf{1}, & \textit{switch } S_{jK} \textit{ turn on} \\ \mathbf{0}, & \textit{switch } S_{jK} \textit{ turn off} \end{cases} \quad (2\text{-}1)$$

, where $j \in \{a, b, c\}$, and $K \in \{A, B, C\}$. Taking into account that phases shall never be short-circuited and the output currents shall not be interrupted, the constraints can be expressed as: (Szczesniak 2013)

$$S_{jA} + S_{jB} + S_{jC} = 1 \quad (2\text{-}2)$$

With these restrictions, the three-phase to three-phase matrix converter allows 27 switching states. The output voltages and output currents can be expressed in matrix form to solve the desired output value for each switching states (Szczesniak 2013).

2.2 Matrix Converter Classification

The classification of MCs is shown in Figure 3.

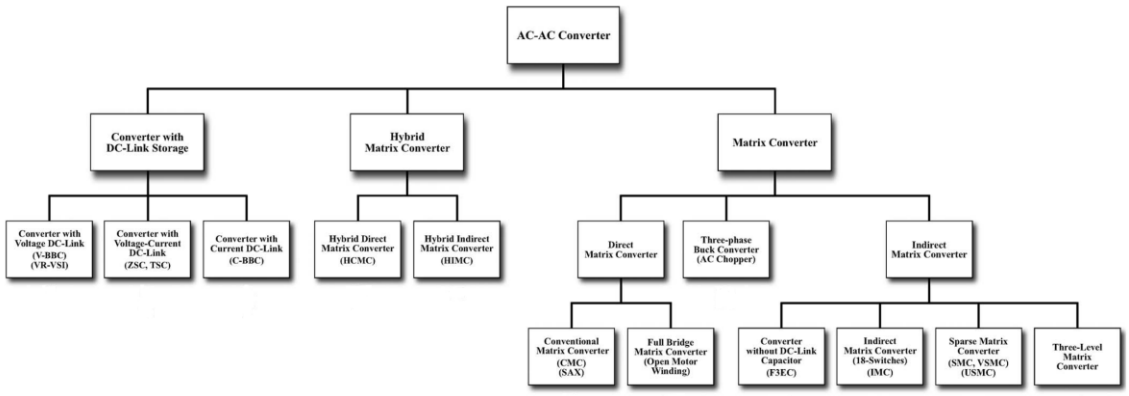

Figure 3: Classification of three-phase AC/AC converter topologies (Kolar et al. 2011).

Mainly three subcategories has been used, Converter with direct DC-link storage, Hybrid Matrix converter and Matrix converters. The forced commutated AC/AC converter is considered as a MC if it does not require an intermediate energy storage power as an essential functional element. (Kolar et al. 2011)

The figure gives a broader idea of the matrix converter classification and the different types of matrix converters is not discussed in detail in this thesis.

2.3 Bi-directional Switch

For the matrix converter, the core of the topology is a bi-directional switch. It is occasionally named also as AC switch. The bi-directional switch can transfer power to both directions; load and the supplying network. The markets offer some bi-directional modules which are listed below:

- Microsemi APTGF90DU60TG
- Dynex DIM400PBM17-A000
- Powerex QIC6508001
- Semikron SKM150GM12T4G

Which are all in module packages. All of them have limitations related to the switching frequency but the manufacturer's data usually doesn't provide the information that is required in switching frequencies over 20 kHz. For this reason, discrete switch components may be used to achieve higher switching frequencies. In Figure 4, it is described how the discrete components may be used to achieve the bi-directional switch.

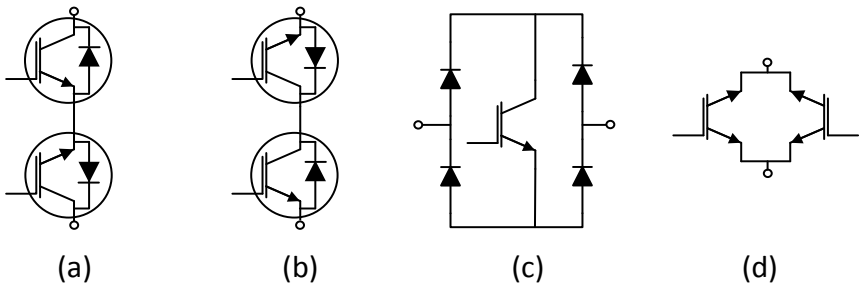

Figure 4: Bi-directional switch arrangements. (a) CE (b) CC (c) DB (d) RB-IGBT.

The shown switch arrangements are as follows: (a) Common Emitter, (b) Common Collector, (c) Diode Bridge, (d) Reverse Blocking IGBT. The most common type of arrangement is the common emitter arrangement and few manufacturers, such as Dynex and Semikron are providing such IGBT modules in the market. The RB-IGBT symbol may vary depending on the source. At the time of this thesis, there was no access to IEC 60747-9, which is a standard covering transistors and semiconductor switches in general.

2.4 Driving of the Bi-Directional Switch

The driving of the IGBT is generally more challenging than driving of FET based switches. The main difference is that IGBT operation requires bipolar gate voltages to drive the gate efficiently. To drive the IGBT to on state, the current is required to be injected to the gate terminal. To achieve this, it is required to drive the gate voltage V_{GE} higher than its given value. In order to turn the IGBT to off-state, a voltage below threshold voltage is applied to the gate terminal. Usually this voltage is negative. However, IGBT can be driven also with voltages from 0 V to 15 V. In general, the bi-directional switch requires usually an isolated driver. For the driver, there are multiple choices to choose such as driver IC's, discrete component solutions and driver modules. (Abjihit, Locher 2009)

To determine the power losses for the driver while driving the IGBT, the power losses can be calculated as follows:

$$\boldsymbol{P_{\mathrm{GATE}} = V_{\mathrm{CC}} Q_{\mathrm{G}} f_{\mathrm{SW}}} \qquad (2\text{-}3)$$

, where V_{CC} is the driver's supply voltage, Q_{G} is the IGBT gate charge and the f_{SW} is the IGBT switching frequency. It is visible that the gate charge is affecting the power losses quite significantly. When designing the drivers for the IGBT, there are significant amount of real-life issues that have to be taken into account. Usually these issues are related to inadequate power supply bypassing or layout is designed improperly. To turn on and off the IGBT, it is basically driving a large capacitive load from the driver's point of view.

To evaluate how much current is required to drive an IGBT, following Equation may be used: (Abjihit, Locher 2009)

$$I = V\frac{C}{t} \qquad (2\text{-}4)$$

, where V is the voltage that is required to turn on the IGBT, which is IGBT dependent parameter. C is the capacitance that is required to charge and the t is time that is used to charge it. If the desired rise/fall time for the gate voltage is from 25 ns to 50 ns, extreme care is required when drawing the layout, such as that traces must be as short as possible. In matrix converters, each IGBT driver requires isolated gate drive. Usually the isolation is done with a transformer. Figure 5 shows the idea of driving a bi-directional switch.

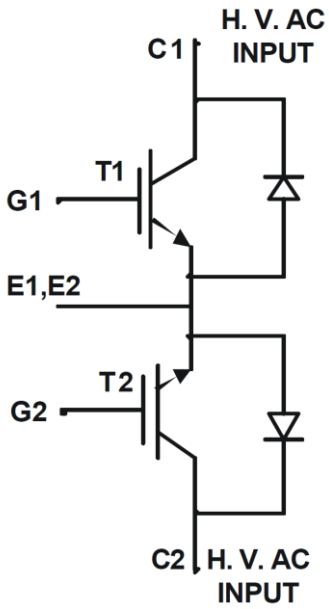

Figure 5: CE driving of the bi-directional switch (Abjihit, Locher 2009).

In this case, the driving circuitry is IC with optical isolators between the controller and the driver IC. The G1 stands for the Gate driver output 1 and G2 is the second gate driver output. The driver emitter terminals are tied together and connected to gate driver IC ground. C1 and C2 are collector signals. (Abjihit, Locher 2009)

2.5 Control of Matrix Converter

The control of matrix converters require two general rules to be addressed:

1. Commutation should not cause short circuit between the input phases
2. Commutation should not cause interrupt in the output current

The second rule can be also deduced from Equation (2-2). This requires the switches to be turned off and on in such a way that the two general rules are obeyed. The reason for this is to prevent the short circuits and sudden current interruptions. To prevent the breaking of two general rules, many methods have been developed, such as dead-time method. The dead time commutation causes high voltage spikes across the switches and forces the use of a snubber circuit. Also, overlap current commutation can be used when inductance is used in order to prevent the rise of the current. This method breaks the general rule over short circuiting the phases but the inductance is used to control the current. Switching frequency is also decreased. These methods are not advanced and thus, more advanced methods are in use. (Szczesniak 2013)

The most common advanced commutation method is four-step method. The timing diagram of the four-step commutation is presented in Figure 6. When $i_L > 0$, it denotes current direction that is from supply towards load. The SaA and SaB are the input phases. SaA1 and SaA2 are the phase A switches forming a bi-directional switch. The SaB1 and SaB2 are the phase B switches. SaA1 and SaB1 are for positive current injection and SaA2 and SaB2 are for negative current injection.

The strategy assumes that when the output phase is connected to an input phase, both of the IGBTs of the bi-directional switch have to be turned on. The method uses current direction to determine the IGBT that is not conducting in each switch. The delay between the switching signals provide the current path for the load current without short circuiting the input phases. (Szczesniak 2013)

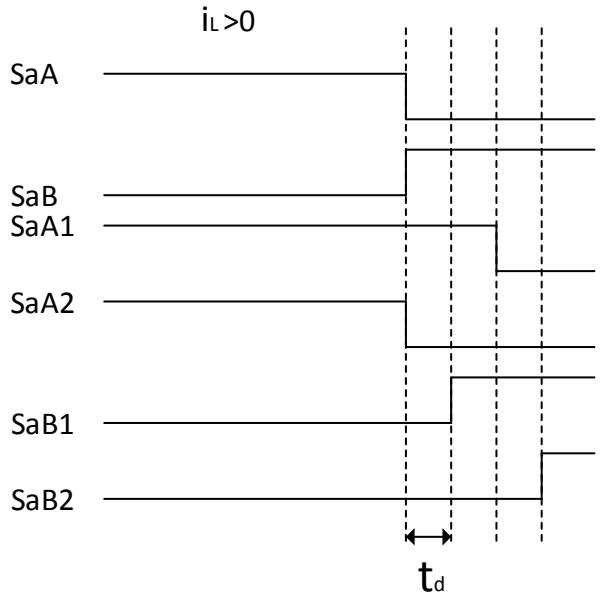

Figure 6: Four-step commutation timing diagram (Szczesniak 2013).

As seen in the timing diagram, the commutation operates in such a manner that the maximum amount of switches to be turned on is only two IGBTs in on-state in all switching states. There could also be only one switch turned on at once. It shall be noticed, that the IGBTs require either body diode or antiparallel diode in this arrangement. Next, the matrix converter modulation techniques are presented in Figure 7.

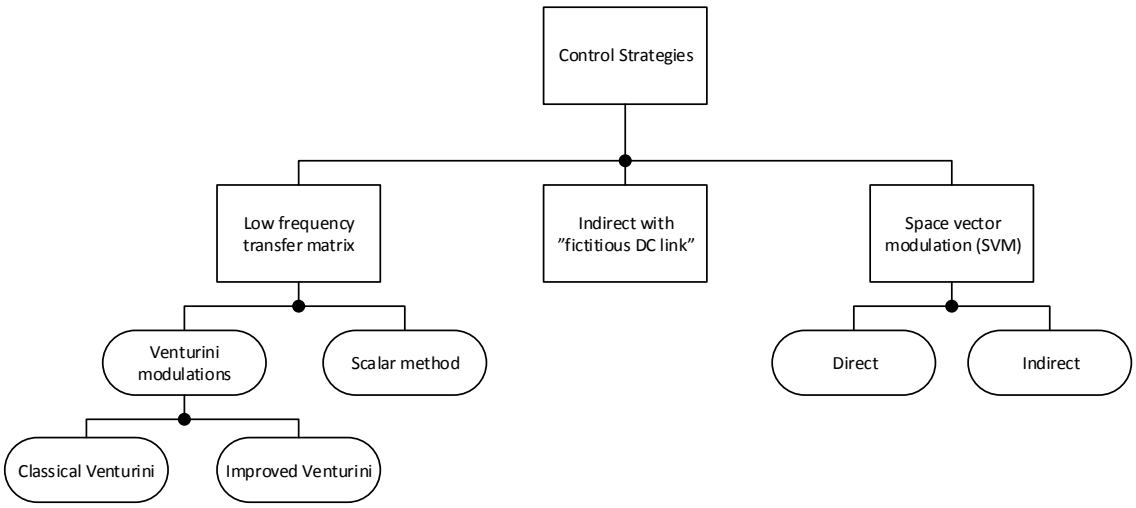

Figure 7: Modulation techniques of the Matrix converter

The figure shows the most well-known modulation techniques for the matrix converters. The classification can be divided into three categories depending on the calculation of the switching states. The modulation techniques are commonly referenced to their

voltage transfer ratios. The voltage transfer ratio is also affected by the converter topology. The most common modulation strategy is probably space vector modulation. (Szczesniak 2013)

2.6 IGBT in Soft Switching Applications

The IGBT losses are dominated by the switching losses. The losses are generated in the switch when the hard switching is used. This means that there is voltage over the switch component while there is current flowing through the switch. In order to reduce these losses, soft switching is used. There are several different means to implement the soft switching as listed below:

- Zero Current Switching (ZCS)
- Zero Voltage Switching (ZVS)

The converter in this thesis will employ zero current switching as it is best suited for IGBT's. In order to achieve the controllable current or voltage in the switch, the switches require a resonant tank circuit. The resonant tank circuit types are listed below:

- Series Resonant Circuit (SRC)
- Parallel Resonant Circuit (PRC)
- LLC or LCC

In this thesis, the series resonant circuit is used as a load. This will generate the resonant current for the switches that can be used to turn them at zero current level. When comparing the hard switching and soft switching, it is useful to see the behavior from the loci shown in Figure 8.

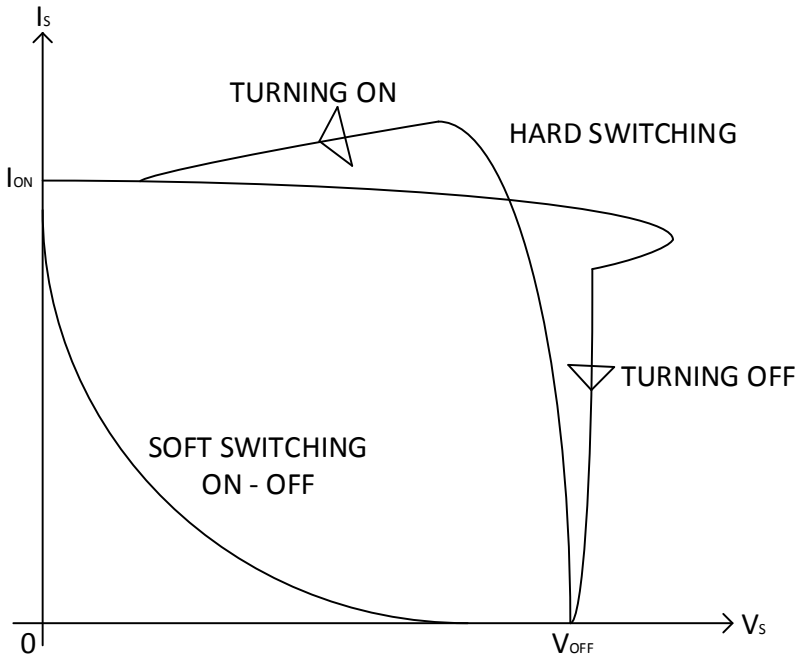

Figure 8: Soft switching versus hard switching.

As seen above, the switching losses are significantly less by using the soft switching. In the ideal situation in soft switching, the current and voltage would travel along the X-Y axes. In this converter, the chosen IGBT was such that it is suited for soft switching applications. The main difference is that the parallel diode has performance better suited for the soft switching operation. In Appendix A it is shown, how the energy loss is decreased if soft switching is used.

2.7 Power Transmission Circuit

The LC resonant circuit is an important part of the resonant converter. In the converter discussed in this thesis the LC circuit is connected in series and the analysis and discussion is only regarding a series resonant circuit. LC circuit is a critical part of the converter while it gives the converter the ability to operate using ZCS and also to utilize the inductive power transfer. The starting point for analysis of a LC circuit can be started from studying how the impedance behaves as a function of frequency. A Bode plot is shown in Figure 9 and it shows a behavior of the series RLC. The reason for using series RLC is that in practice, there is always at least parasitic resistive part in the circuit. At the resonant frequency the impedances of the inductor and the capacitor are equal and cancelling each other, therefore, the impedance reduces to the resistive part.

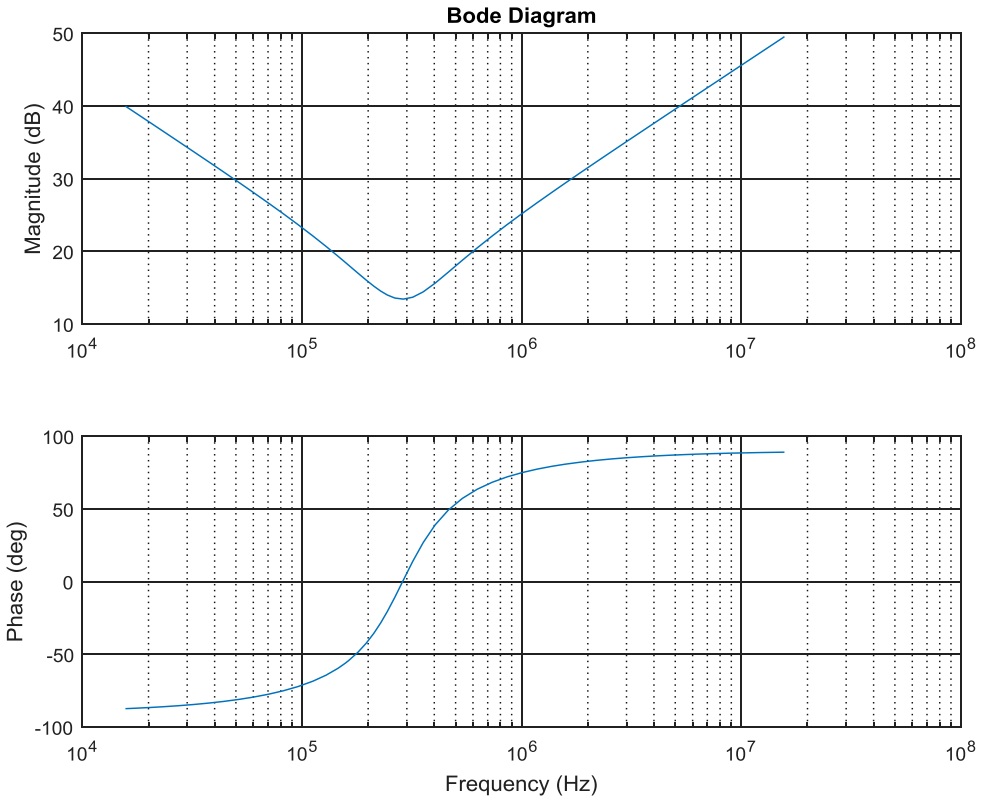

Figure 9: Bode plot for RLC circuit.

The resonant frequency can be seen at the point where the magnitude is at its minimum or the phase is at zero degrees.

The Bode plot was calculated with the following values

- L = 30 µH
- C = 1 µF
- R = 4.7 Ω

The impedance of the LC circuit at the resonant frequency can be obtained with the following Equation:

$$\boldsymbol{Z = j\omega L + \frac{1}{j\omega C} + R} \quad (2\text{-}5)$$

And the resonant frequency can be derived from the Equation, setting the reactive parts to zero (2-5)

$$f_0 = \frac{1}{2\pi\sqrt{LC}} \quad (2\text{-}6)$$

In this frequency, the impedance equals resistive part. In the WPT applications, the figure-of-merit (FOM) of the transmitter coil as a function of power transmission efficiency is defined by

$$\mathbf{FOM} = \boldsymbol{kQ} \quad (2\text{-}7)$$

, where k is the coupling factor and Q is the quality factor of the inductor. This leads to the interpretation that the system power transmission efficiency of the coils increases when coupling is increased or quality factor increases. Quality factor of the inductor is calculated as follows

$$\boldsymbol{Q_i = 2\pi \frac{W_{Li}}{P_{\text{loss}}/f_0} \approx \frac{\omega_o L_i}{R_i}} \quad (2\text{-}8)$$

, where:

- i 1 (primary), 2 (secondary)
- W_{Li} Peak inductor energy stored in inductor L_i
- P_{loss} Average power loss of the W_{Li}
- f_0 , ω_o Resonant frequency
- R_i Parasitic resistance in series with L_i

The quality factor together with the coupling factor k defines the power transfer efficiency and they define the power transfer efficiency as follows

$$\eta_{max} \approx 1 - \frac{2}{kQ} \quad (2\text{-}9)$$

Therefore, a high transmission efficiency can be achieved if large coils with a high magnetic coupling are used, which leads to a low power density. Higher power density could be achieved by using smaller coils but it decreases the transfer efficiency. The maximum efficiency can be achieved only if the load is optimally matched to the receiver inductance according to the following equation

$$\gamma_{SS,OPT} = \frac{1}{Q_2}\sqrt{1 + k^2 Q_1 Q_2} \quad (2\text{-}10)$$

, where $\gamma_{SS,OPT}$ is the load matching factor. For equal and large coil quality factors Q_1 and Q_2 the optimal load matching factor can be approximated to be

$$\gamma_{SS,OPT} \approx k \quad (2\text{-}11)$$

, and since in this thesis, a series resonant circuit is used, the capacitor can be calculated using the following equation

$$C_i = \frac{1}{\omega_0^2 L_i} \quad (2\text{-}12)$$

, where i is 1 for primary and 2 for secondary. By selecting the capacitor accordingly it leads to the highest power transmission efficiency. Equation can be also noticed to be the same as (2-6) for the resonant frequency. The resonant circuit for the converter was chosen to be a series compensation topology. Reason for this is that at higher power levels the size of the coil is typically increased to obtain larger surface area for a cooling system. When the coil size increases, the inductance increases. In a parallel compensated topology, low inductance is required in order to maintain the optimal values for the circuit parameters. (Bosshard et al. 2015)

The inductance calculations are shown in Chapter 3.2.1 which shows that by increasing the size, the realizable inductance increases.

2.8 Proposed Direct AC/AC Converter

The proposed AC/AC converter is shown in Figure 10. The secondary circuit is not in the focus of this thesis, but it is shown there while the final purpose of the converter is to include wireless power transfer. The secondary power stage is going to be somewhat identical to the primary power stage. The requirement for the end product is that the converter shall enable bi-directional power flow.

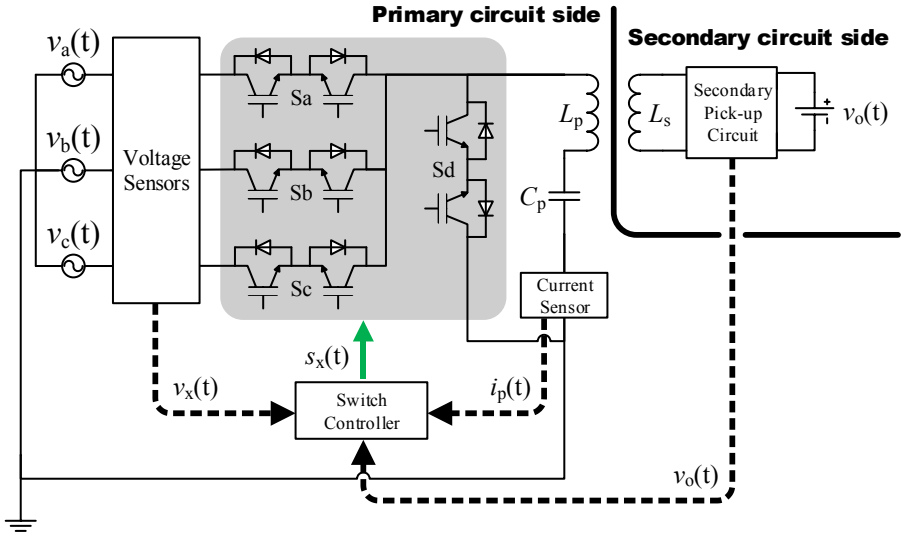

Figure 10: Proposed AC/AC Resonant Converter.

In Figure 10, the dashed black arrows are showing the feedback signals for the controller and the green solid arrow is showing the control signals. The control signals are connected to the bi-directional switch components S_a, S_b, S_c, S_d. The voltage sensors are measuring the phase voltages and the current sensor is measuring the current direction in the primary load circuit. Secondary pick-up circuit is giving the indication of the battery voltage back to the switch controller that makes the decision on the energy injection into the resonant circuit.

The feedback from the secondary is not galvanically coupled and is using RF communications to achieve the connection. The switches could be according to the power requirements but in the first prototype, they are IGBTs in TO-247 package. In the future, they can be replaced by more efficient components such as SiC MOSFET. The use of multi-level configurations would also enable even higher switching frequencies. The voltage measurement is based on measuring the absolute maximum voltage of the phase. The phase voltage that has the highest absolute value at each measured moment is selected to be used to inject the power into the load.

The primary circuit consists of the primary inductance L_p and the primary capacitance C_p. The secondary inductance L_s in accordance with the primary inductance are forming the transmitter-receiver pair. The primary applications for the converter are Electric Vehicle / Hybrid Electric Vehicle charger but the converter may be used in any application requiring wireless power transfer. (Kusumah, Vuorsalo & Kyyrä 2015)

2.9 Thermal Considerations

Thermal issues in converters are considering all components in the converter. Most of all, switching components are under greatest stress of all components. Other components that are under thermal stress are magnetics components, capacitors and resistors. The PCB design also affects the thermal performance of the system. Thermal cycles and high temperatures are the main reason for power semiconductors to fail prematurely. Thermal cycles also wear the thermal interface material (TIM) if poorly designed.

To ensure the lifetime of the power electronics device, proper thermal management is a key factor. Special care should be taken into account when designing proper thermal interface. Proper connection between the components and the heat sink must be taken into account. (Schulz 2013) Thermal interface material is also crucial for the thermal performance of the switches. The TIM is the material between semiconductor and heatsink. This layer is needed to achieve proper and long-term stable transfer of the heat from the semiconductor case to heatsink. (Schulz 2014)

2.10 Alternative Switch Components

In the future, the switch components could be replaced by SiC MOSFET components. The main reason for this is, it enables greater switching frequency and higher power density.

In the field of research, there has been results that showed inverter efficiency to be increased from 96.5 % to 98.5 % with 40 kHz switching frequency when Si IGBT was replaced with SiC MOSFET module. The same study also showed improvements in energy loss of the components shown in Table 1.

Table 1: Comparing SiC MOSFET to Si IGBT (Gangyao et al. 2013)

Loss [mJ]	Cree SiC MOSFET	Infineon Si IGBT
E_{ON}	2.47	8.78
E_{OFF}	1.28	8.78
E_{REC}	0.53	5.93

E_{ON} is the turn-on energy loss, E_{OFF} is the turn-off energy loss and E_{REC} is the energy loss of the body diode during the reverse recovery. Also, the study shows improvements in power losses at 40 kHz switching frequency shown below:

- Si IGBT 360.8 W
- SiC MOSFET 114.47 W

And finally the study shows that the efficiency of the inverter was always better with SiC MOSFET than using Si IGBT and the efficiency difference between IGBT and MOSFET increases when switching frequency increases. (Gangyao et al. 2013) Other newer research compares Si BiMOSFET, Si IGBT and SiC MOSFET. The research shows that the losses with BiMOSFET and IGBT are 5-6 times higher than the SiC MOSFET and the losses of SiC MOSFET could be decreased by lowering the gate resistance. However, this does not apply for the BiMOSFET and IGBT. (Hazra et al. 2015)

The comparison study also incorporates zero voltage switching and found that the SiC MOSFET operates without any switching losses in the ZVS mode. Also, the conclusion provides that the power ratings of the same converter using SiC MOSFET could be increased to 10 to 15 fold over the conventional converters using Si IGBT or Si BiMOSFET. Switching frequency could be also increased 7 to 10 times higher. (Hazra et al. 2015)

In the future, the switch components could also be embedded in the PCB. One such manufacturer is Schweizer with their P^2 pack technology. (Schweizer 2015)

3 Design

This chapter describes the design of the proposed converter. It was decided that in a practical design, a resistor is included in the LC circuit in order to dissipate some amount of heat. The reason for this was that during the simulation of the circuit, it was found out that the voltages for the inductor and the capacitor may increase over 1 kV which makes the component stresses high for each component. This chapter contains analytical solutions for the RLC circuit to solve the component values that were used during the prototype realization as well as the other values that were important in the realization. Some component values are not calculated but chosen after findings during testing of the converter.

3.1 Technical Description

The main system block diagram is presented in Figure 11 and the concept schematic is shown in Appendix A.

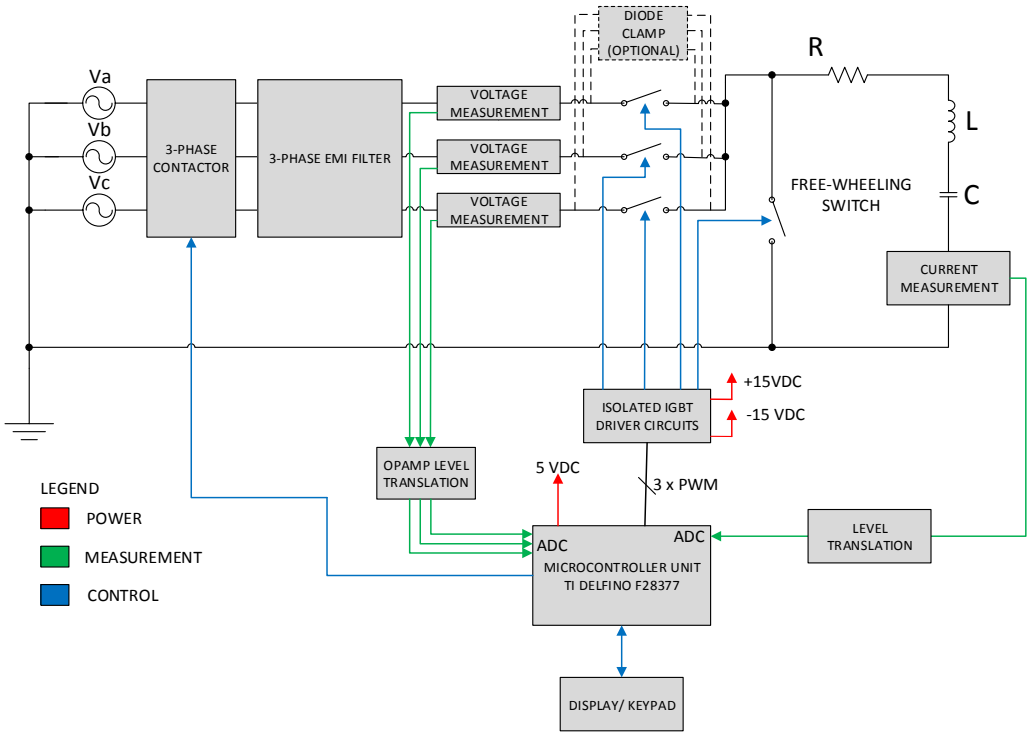

Figure 11: Block diagram of the converter.

Level translation is done with operational amplifiers and resistor divider. The main reason for this is due to the microcontroller ADC input can input 3 VDC maximum. Contactor is used for safety reasons in order to control the connection to the three-phase network during fault situations. Free-wheeling circuit does not employ any safety

circuit in the first phase of prototype design due to a controlled testing environment. Diode clamp or snubber circuit may be required for the switch components but they are left out from the first prototype design and may be added after findings during testing of the converter. The main parameters of the converter are listed below:

- Input voltage 3-phase 230 VAC, 50 Hz
- Resonant frequency f_{RES} 30 kHz…100 kHz
- Nominal output power 8 kW ±1 %
- Overall efficiency > 90 %
- Switching frequency f_{SW} According to f_0

Figure 12 shows the commutation strategy of the proposed converter. The converter operation is based on current injection to the load when required.

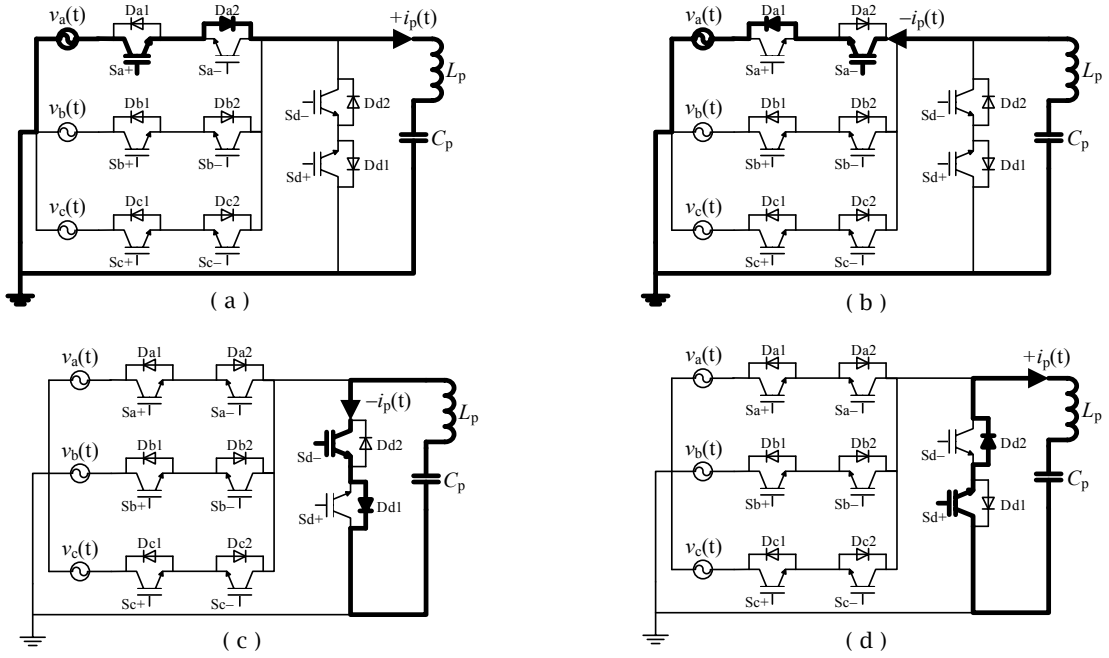

Figure 12: Proposed converter commutation scheme. (a) Positive current injection from phase a to the load. (b) Negative current injection from phase a to the load. (c) Negative current free-wheeling. (d) Positive current free-wheeling. (Kusumah, Vuorsalo & Kyyrä 2015)

The switching is based on the resonant frequency of the load LC circuit. For IGBT gate switching, the converter controller requires current sign information and the absolute values of phase voltage magnitudes. The current is injected when the load requires current to be injected, where the reference current is pre-defined by the control

algorithm. If the current injection is not needed, the free-wheeling switches Sd- and Sd+ are used to enable bi-directional current flow. (Kusumah, Vuorsalo & Kyyrä 2015)

3.2 Primary Resonant Circuit Design

The primary resonant circuit consists of a resistor, an inductor and a capacitor. The inductor was chosen to be manufactured manually at the laboratory while this enables more flexibility during the prototyping in finding a suitable value for inductance. The values for the primary resonant circuit were not exactly defined in the design phase due to the fact that the project needed multiple values to test. The testing phase describes the findings related to the inductor.

3.2.1 Inductor

Analytical approach to define inductor is presented in this section. Inductor shape was chosen to be circular loop due to the applications that has been studied in wireless power transfer research papers (Imura, Hori 2011).

The inductor was chosen to be air cored. The benefit of the air core inductor is that it is accurate and it is not influenced by the magnetic material properties. They have also uses in resonant circuit applications. To evaluate the inductance of the coil to be built, it is chosen to use the general case Equation. The inductance is evaluated based on equation from page 305 of (Van den Bossche, Valchev 2005).

$$L = \frac{\mu_0 \mathrm{N}^2 \pi \mathrm{a}^2}{\mathrm{b}} \frac{1}{1 + 0.9(\mathrm{a/b}) + 0.32(\mathrm{c/a}) + 0.84(\mathrm{c/b})} = \quad (3\text{-}1)$$

, where

- $\mu_0 = 4 * \pi * 10^{-7}\ {}^{\mathrm{Vs}}/_{\mathrm{Am}}$
- N = Number of turns

, and Figure 13 shows the dimensions for a, b and c.

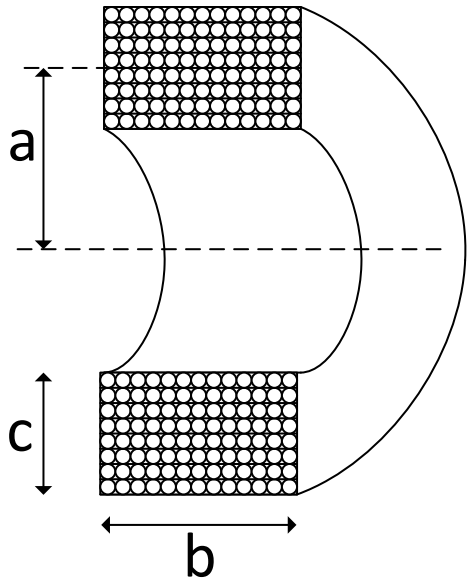

Figure 13: Inductor measures in general case.

Now, with following design specification, the inductance can be obtained:

- a 6.75 cm
- b 2 cm
- c 1.5 cm
- N 12

The inductance of 27.3 µH is obtained using Equation (3-1). Next, skin depth of the current is required to be defined to obtain the diameter of the practical copper wire. The skin depth can be calculated with the following equation that employs the wide frequency eddy current losses method (Van den Bossche, Valchev 2005).

$$\delta = \sqrt{\frac{2\rho_{Cu}}{\omega\mu}} \qquad (3\text{-}2)$$

, where

- ρ_{Cu} $1.68 * 10^{-8}$ Ωm
- ω $2\pi f_{\mathrm{SW}}$
- μ_{r} 1, for air.
- μ $\mu_0 * \mu_{\mathrm{r}} = 4 * \pi * 10^{-7}\ {}^{\mathrm{Vs}}/_{\mathrm{Am}} * 1$

For a penetration depth at the frequency of 30 kHz and temperature of 20℃,

$$\delta_{\mathrm{w}} = \sqrt{\frac{2 * 1.68 * 10^{-8}\ \Omega m}{2 * \pi * 30\ \mathrm{kHz} * 4 * \pi * 10^{-7}\ {}^{Vs}/_{Am}}} \approx 0.38\ \mathrm{mm} \qquad (3\text{-}3)$$

So, at 30 kHz frequency, the copper wire thickness is not required to be more than 0.4 mm. It is obvious that for higher currents, the obtained skin depth is not suitable. In order to obtain the appropriate coil winding, litz wire should be used. There are also indications that the litz wire usage increases the overall efficiency of the WPT system (Mizuno et al. 2012).

Litz wire is a wire that consists of a bundle of magnet wires and insulating material. Standard wire configurations are 7, 19, 25, 37, 60, 100, 200, 400 but they vary depending on the manufacturer. One manufacturer data can be found from Appendix G.

The analysis for the litz-wire can be obtained from the book (Kazimierczuk 2014, p. 348). After obtaining the skin depth for the frequency, the calculation can be done using some assumptions. The reason for the assumptions is that the wire manufacturer does not provide the exact information.

$$\mathrm{N_{ll}} = \mathrm{N_l}\sqrt{\mathrm{k_{litz}}} = 2 * \sqrt{400} = 40 \qquad (3\text{-}4)$$

Where

- $\mathrm{N_{ll}}$ Effective number of wire layers
- $\mathrm{N_l}$ Number of wire bundle layers = 2
- $\mathrm{k_{litz}}$ Number of wire strands in the litz wire = 400

And assuming the porosity factor (or fill factor) of

$$\eta_{\mathrm{ff}} = \frac{\mathrm{d}}{\mathrm{p}} = 0.7 \qquad (3\text{-}5)$$

, where

- η_{ff} Porosity factor
- d Diameter of the wire strand
- p Distance from strand midpoint to strand midpoint

The porosity factor is usually less than 0.8 due to the fact that litz wire includes nylon textile or yarn to provide insulation and strength. Using the assumption, a normalized optimum strand diameter is obtained as follows,

$$\frac{d_{lopt}}{\delta_w} = \sqrt[4]{\frac{45}{\eta^2 \left(\frac{\pi}{4}\right)^3 \left(5N_{ll}{}^2 - 1\right)}} = \sqrt[4]{\frac{45}{0.7^2 \left(\frac{\pi}{4}\right)^3 (5 * 40^2 - 1)}} = 0.36979671 \ldots \quad (3\text{-}6)$$

Subscript w indicates winding and the optimum wire diameter is therefore:

$$d_{lopt} = \delta_w * 0.36979671 = 0.15 \text{ mm} \quad \textbf{(3-7)}$$

And from the Appendix G, it is obtained that the selection could be AWG38 0.10 mm with 420 strands. The outer diameter without insulation is 2.95 mm. In order to calculate the maximum porosity factor, it would require information of insulated wire diameter which is available only upon request. The maximum porosity factor can be obtained with the following equation,

$$\eta_{max} = \left(\frac{d_l}{d_o}\right)^2 \quad (3\text{-}8)$$

, where

- d_l Wire diameter without insulation
- d_o Wire diameter with insulation

Since the diameter with insulation is not provided in the datasheet, $\eta_{max} = 0.75$ is assumed. Next, the DC resistance of the litz wire is calculated with equation

$$R_{wDC} = \frac{\rho_{Cu}}{\pi k d_l^2} = \frac{1.68 * 10^{-8} \Omega m}{\pi * 40 * (0.1 * 10^{-3} m)^2} = 13.37 \text{ m}\Omega \quad (3\text{-}9)$$

And the normalized strand diameter is obtained with equation

$$\frac{d_l}{\delta_w} = \frac{0.1 \text{ mm}}{0.3766 \text{ mm}} = 0.266 \quad (3\text{-}10)$$

AC-to-DC resistance ratio is,

$$F_R \approx 1 + \frac{\left(5N_l{}^2 k - 1\right)}{45}\left(\frac{\pi}{4}\right)^3 \eta_{max}{}^2 \left(\frac{d_l}{\delta_w}\right)^4 = \quad (3\text{-}11)$$

$$1 + \frac{5 * 2^2 * 420 - 1}{45}\left(\frac{\pi}{4}\right)^3 * 0.75^2 * 0.266^4 = 1.25$$

And the litz-wire AC resistance is,

$$R_{\mathrm{w}} = F_{\mathrm{R}} R_{\mathrm{wDC}} = 1.25 * 13.37\ \mathrm{m\Omega} = 16.75\ \mathrm{m\Omega} \quad (3\text{-}12)$$

By assuming $I_{\mathrm{winding}} = 10\ A$, the power loss in the winding is,

$$P_{\mathrm{w}} = \frac{R_{\mathrm{w}} {I_{\mathrm{winding}}}^2}{2} = 837.48\ \mathrm{mW} \quad (3\text{-}13)$$

Current carrying capacity is evaluated in Chapter 4.1 which also defines the maximum allowable current in the wire. (Kazimierczuk 2014)

3.2.2 Capacitor

The capacitor was selected to be Cornell Dubilier SFA66T1K156B-F. In this application, capacitor is used in resonant circuit. Therefore the losses have to be evaluated by solving the Fourier-series of the current. When the current components are known, the power loss can be calculated with the following Equation

$$P_{\mathrm{H}} = \sum_{\mathrm{n}} R_{\mathrm{n}} I_{\mathrm{n}}^2 \qquad (3\text{-}14)$$

, where

- R_{n} ESR at the desired frequency.
- I_{n} Current magnitude at nth component
- n Frequency component number.

In this case, the manufacturer did not give the ESR and the dissipation factor is given to be < 0.1 %. This can be interpreted as $\tan \delta_n = 0.001$. Now, the resistance at a certain frequency can be evaluated as follows,

$$R_{\mathrm{n}} = \frac{1}{\omega_{\mathrm{n}} C} \tan \delta_{\mathrm{n}} \qquad (3\text{-}15)$$

and finally the internal temperature can be calculated as follows,

$$T_{\mathrm{D}} = R_{\mathrm{th}} P_{\mathrm{H}} + T_{\mathrm{A}} \qquad (3\text{-}16)$$

, where

- T_{D} Internal temperature
- R_{th} Thermal resistance of the capacitor
- T_{A} Ambient temperature

R_{th} is not always given but it can be deduced by calculating the power loss in nominal operating point. The deduction can be checked by extrapolating the graphs in the datasheet. (Niiranen 2007)

To define the capacitor losses, following specifications are required to be known (CDE 2015), (Cornell Dubilier 2015):

- Maximum AC voltage rating 400 V
- Maximum operating temperature 70 ℃
- Operating frequency 30 kHz
- Dissipation factor < 0.1 %
- Maximum current 30 A
- Capacitance 1 µF
- Thermal resistance 17.5 $\frac{℃}{W}$

The thermal resistance was asked directly from CDE via e-mail. In this application, the input current can be simplified to be sinusoidal, so the Fourier series is truncated to the first component of the series. The ESR is obtained first by calculation:

$$R_{\mathrm{n}} = \frac{1}{2 * \pi * 30\ \mathrm{kHZ} * 1\mu\mathrm{F}} * 0.001 = 0.531\ \mathrm{m\Omega} \quad (3\text{-}17)$$

And the power loss can be calculated

$$P_{\mathrm{H}} = 0.531\ \mathrm{m\Omega} * (30\ \mathrm{A})^2 = 477.9\ \mathrm{mW} \quad (3\text{-}18)$$

Finally, the temperature at the room temperature (25 ℃)

$$T_{\mathrm{D}} = 17.5\frac{℃}{W} * 477.9\ \mathrm{mW} + 25\ ℃ = 33.36\ ℃ \quad (3\text{-}19)$$

, which is below the maximum operating temperature and the operating point is suitable for the capacitor.

3.2.3 Resistor

The resistor of the resonant circuit is to provide the current limit for the LC circuit. It creates damping for the circuit. The resistor in this application is chosen to be wire wound power resistor and its resistance is not critical in this application. Therefore, its detailed value is not considered. The sole purpose is to include a power consuming element into the resonant circuit for the prototype testing. Power rating for the prototyping resistor shall be quite large due to the simulation findings in the reference (Kusumah, Vuorsalo & Kyyrä 2015). The power rating was decided to be at least 1 kW in order to reduce the risk of fire. Final product does not have resistor in the load circuit.

3.3 Switching Component

The switching component in the first prototype was chosen to be an IGBT. The model is Infineon IHW40N120R3 which is suitable for resonant switching applications such as induction stove. The main characteristics are shown in Table 2.

Table 2: Switch component properties (Infineon 2015)

Feature	Value
Collector-emitter voltage	1200 V maximum
DC collector current / Pulsed I_C at 25 °C	80 A / 120 A maximum
Power dissipation at 25 °C	429 W
Input capacitance	2108 pF
Gate charge	335 nC

The loss calculation is done for a certain input level which is not necessarily the test input level. However, it is obvious that the power losses need to be defined for a certain output current in order to obtain the guidelines for the component temperatures under greater stress. The power losses of the IGBT consists of conduction losses, switching losses and leakage losses. Leakage losses are usually negligible and can be omitted from the calculations. (Graovac, Pürschel 2009) Both IGBT and the body diode losses has to be calculated separately.

In order to calculate the losses, following assumptions are made:

- Switching frequency 40 kHz
- Collector current 40 A
- Duty cycle 0.5
- Ambient temperature 25 °C

The Switching frequency of 40 kHz and with a duty cycle of 0.5 results $t_{on} = t_{off} =$ 12.5 µs. The duty cycle is 0.5 for the simplicity made for the calculation of the losses. In normal operation of the prototype, duty cycle will be changed according to the load current and the magnetic circuit arrangement.

From the datasheet (Infineon 2015), following values have been obtained by using methods presented in (Graovac, Pürschel 2009):

- $E_{\mathrm{ION}} = E_{\mathrm{IOFF}} = 0.48\ \mathrm{mJ}$
- $V_{\mathrm{D0}} = 1.2\ \mathrm{V}$
- $V_{\mathrm{CE0}} = 1.2\ \mathrm{V}$
- $r_{\mathrm{C}} = \frac{\Delta V_{\mathrm{CE}}}{\Delta I_{\mathrm{C}}} = \frac{1.1\ \mathrm{V}}{90\ \mathrm{A}} = 12.2\ \mathrm{m\Omega}$
- $r_{\mathrm{d}} = \frac{\Delta V_{\mathrm{D}}}{\Delta I_{\mathrm{D}}} = \frac{1.1275\ \mathrm{V}}{55\ \mathrm{A}} = 20.5\ \mathrm{m\Omega}$
- $R_{\mathrm{thJC}} = 0.35\ {}^{\mathrm{K}}/_{\mathrm{W}}$
- $R_{\mathrm{thJA}} = 40\ {}^{\mathrm{K}}/_{\mathrm{W}}$

The power losses can be evaluated by calculating the conduction losses and switching losses separately. The switching losses for soft switching can be found from the datasheet if the voltage derivative suits for the needs. In this calculation, it is assumed that the derivative of voltage is 150 V/µs and that the current is sinusoidal. The IGBT instantaneous conduction losses are:

$$\boldsymbol{P_{\mathrm{CI}} = V_{\mathrm{CE0}} I_{\mathrm{CAV}} + r_{\mathrm{C}} I^2_{\mathrm{CRMS}} = 1.2\ \mathrm{V} * 40\ \mathrm{A} + 12.2\ \mathrm{m\Omega} * \left(\frac{40\ \mathrm{A}}{\sqrt{2}}\right)^2 = 57.76\ \mathrm{W}} \quad (3\text{-}20)$$

Diode instantaneous conduction losses are:

$$\boldsymbol{P_{\mathrm{CD}} = V_{\mathrm{D0}} I_{\mathrm{DAV}} + r_{\mathrm{d}} I^2_{\mathrm{DRMS}} = 1.2\ \mathrm{V} * 40\ \mathrm{A} + 20.5\ \mathrm{m\Omega} * \left(\frac{40\ \mathrm{A}}{\sqrt{2}}\right)^2 = 64.40\ \mathrm{W}} \quad (3\text{-}21)$$

Switching losses of the IGBT can be calculated as follows,

$$P_{\mathrm{SWI}} = f_{\mathrm{SW}} * (E_{\mathrm{ION}} + E_{\mathrm{IOFF}}) = 40\ \mathrm{kHz} * 0.96\ \mathrm{mJ} = 38.4\ \mathrm{W} \quad (3\text{-}22)$$

The reverse recovery energy is approximated from the datasheet to be $E_{DRR} = 0.33$ mJ. Majority of diode losses are caused by the reverse recovery during switching. Diode switching losses are

$$P_{\mathrm{SWD}} = f_{\mathrm{SW}} * (E_{\mathrm{DRR}}) = 40\ \mathrm{kHz} * 0.33\ \mathrm{mJ} = 13.2\ \mathrm{W} \quad (3\text{-}23)$$

, and the losses can be calculated for IGBT and diode by adding losses during conduction and switching:

$$\boldsymbol{P_{\mathrm{I}} = P_{\mathrm{CI}} + P_{\mathrm{SWI}} = 57.76\ \mathrm{W} + 38.4\ \mathrm{W} = 96.16\ \mathrm{W}} \quad (3\text{-}24)$$

$$\boldsymbol{P_D = P_{CD} + P_{SWD} = 64.40\ W + 13.2\ W = 77.60\ W.} \quad (3\text{-}25)$$

Temperature can be calculated when the heatsink thermal resistance is known to be $R_{thSA} = 8.6$ K/W (Ohmite 2015). The connection between the heatsink and the IGBT is assumed to be ideal and the temperature is calculated as follows,

$$T_C = (P_I + P_D) * (R_{thJC} + R_{thSA}) + T_A = 173.76\ W * 8.95\ {}^{K}/_{W} + 25\ ℃ \approx 1580\ ℃ \quad (3\text{-}26)$$

This is obviously too much for the IGBT in order to operate under such conditions. This means that the first prototype will not be operated at 40 kHz and 40 A, but instead something less that is found appropriate during the testing. If the IGBT would operate under hard switching control, the power losses would be increased significantly.

3.4 IGBT Driver

IGBT driver for the project was chosen to be Power Integrations 2SC0108T. It is a two channel IGBT driver that is suitable for IGBTs connected in series. It features two input channels that can be operated individually in direct-mode or in half-bridge mode. Some of the features are listed in Table 3 below.

Table 3: IGBT driver features

Feature	Value
Gate Current	±8 A, 1 W / channel
Blocking Voltage	1700 V
Control Inputs	3.3 V…15 V
Supply Voltage	0 V…16 V
Switching Frequency	50 kHz max
Maximum Gate Charge	6.3 µC

As mentioned, the gate signals can be driven either in direct-mode or half bridge-mode. The direct-mode can drive gates independently from each other and thus it is suitable for this application. The risk in the direct-mode is that the synchronous or overlapping timing could short circuit the phases. In the half-bridge mode, the B input is an enable signal for the A input. The gate signals have defined dead-time between the switching. The dead-time can be chosen by the user by selecting a certain value of resistor between a pin and ground in the driver circuitry.

Since there are very little literature about the IGBT driving with the bi-directional switch, the behavior was simulated with OrCAD PSPICE to ensure a correct operation in the actual converter. The simulated circuit is shown in Figure 14. In the figure, the drive circuit is provided with ±15 V drive voltage and the driving is done with pulsed voltage source. The frequency is 40 kHz, and the load is 1 ohm. The model for the IGBT's are selected based on the models that can be found from the default OrCAD libraries. It is not critical to implement the circuit with the selected IGBT's but the simulation requires an IGBT with body diode. The circuit shows that the emitters are connected together enabling the common emitter arrangement. The results are shown in Figure 15 and Figure 16, where the first figure shows the switched input voltage for one phase and the latter figure shows the switching signals for the IGBT gates. The gate signals operate in counter phase mode which simulates the direct-mode in the driver.

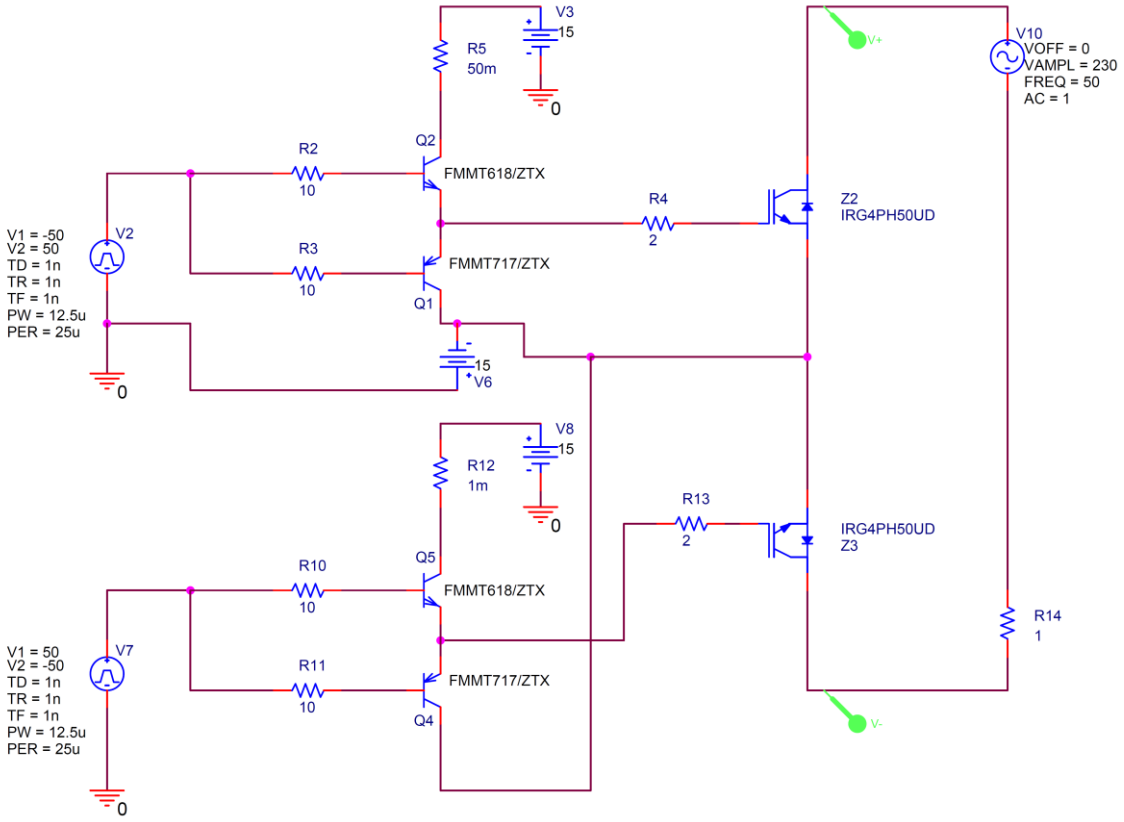

Figure 14: Simulation for Bi-directional switch drive.

Figure 15: Switched input voltage. Horizontal scale: 0.2 ms/div, Vertical Scale: 20 V/div. Vmin = -300 V, Vmax = 300 V.

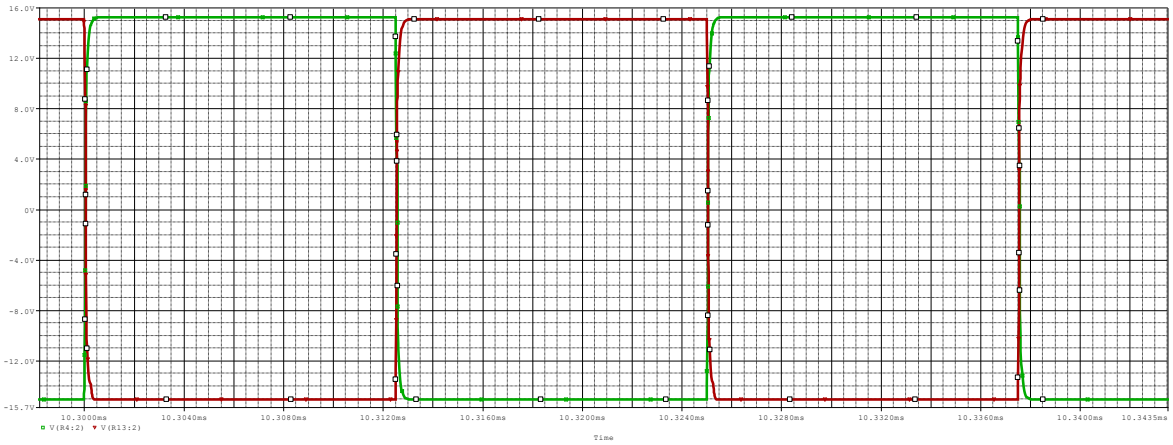

Figure 16: Gate Drive signals. GREEN = upper switch, RED = lower switch. Horizontal scale: 20 µs/div, Vertical Scale: 1 V/div. Vmin = -15.7 V, Vmax = 16.0 V.

The power loss in the gate resistor is shown in Figure 17. The green line represents the RMS power that is 763.4 mW. The red waveform represents pulsed power. This is well below the maximum power of 1 W which was specified for the IGBT driver. The datasheet provides information that it should not be exceeded at any time. However, the simulation model is not accurate model of the IGBT driver and only RMS power is taken into consideration.

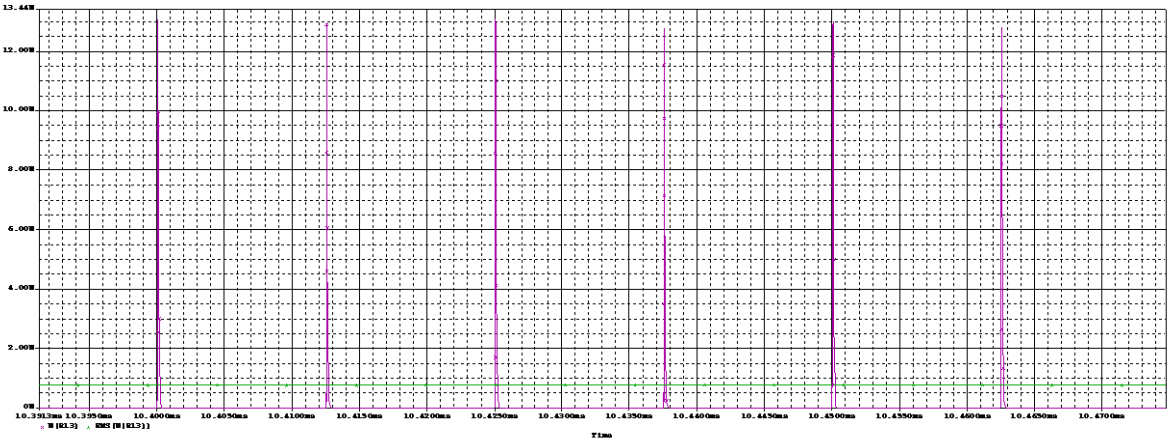

Figure 17: Detailed gate driver resistor power loss, RED = Pulsed, GREEN = RMS power. Horizontal scale: 1 µs/div, Vertical Scale: 0.5 W/div. Pmin = 0 W, Pmax = 13.44 W.

3.5 Microcontroller

The microcontroller for the converter was chosen to be Texas Instruments' TMS320F28377D Dual-Core Delfino Microcontroller. The MCU includes dual core architecture with two TMS320C28x 32-bit CPU's. Some of its features are listed in Table 4.

Table 4: MCU main features (Texas Instruments 2015)

Feature	Value
Frequency	200 MHz
RAM	204 kB
Flash	1024 kB
CLA	2
TMU	2
VCU II	2
FPU	Yes
ADC modules	4
ADC resolution	16 bit/12 bit
ADC conversion time 16b/12b	910 ns / 286 ns
PWM channels	24

The MCU includes the CLA (Control Law Accelerator), TMU (Trigonometric Math Unit) and VCU II (Viterbi/Complex Math Unit) with floating point unit. The MCU is going to be used to control the complete converter. The Texas Instruments indicates in their documents that the MCU could be used for matrix converters.

The dual-core architecture and the CLA together enables the converter to drive other time-critical tasks in onecore while the other core can focus on calculating the gate signals of the switches. Control Law Accelerator is a 32-bit floating-point math unit. The CLA also enables the MCU to read ADC samples in "just-in-time" manner, which means that the ADC sample-to-output delay decreases significantly compared to MCUs without CLA. It also frees up the main CPU to do other tasks while the CLA performs time-critical tasks. This also enables the control loop frequency.

The ADC includes selectable resolution of 12 bits or 16 bits. The start of conversion (SOC) can be configured by the user and the trigger sources can be selected from multiple sources. The ADC uses SAR (Successive Approximation Register) and the ADC

modules include single sample-and-hold circuit. Input voltage range that can be converted is between the reference voltages VREFHI and VREFLO. These voltages are limited by maximum limits shown as follows:

- VREFHI Analog supply voltage
- VREFLO Analog ground voltage

Analog supply voltage is usually 3.3 VDC and its maximum is 3.47 VDC. The module is designed for simultaneous sampling or each module operating independently. ADC clock is defined through system clock and a pre-scale value in the ADC control register. The system clock is defined by the external or internal clock source. The clock configuration for the MCU is done in the initialization phase. (Texas Instruments 2015)

The block diagram of the microcontroller is presented in Figure 18.

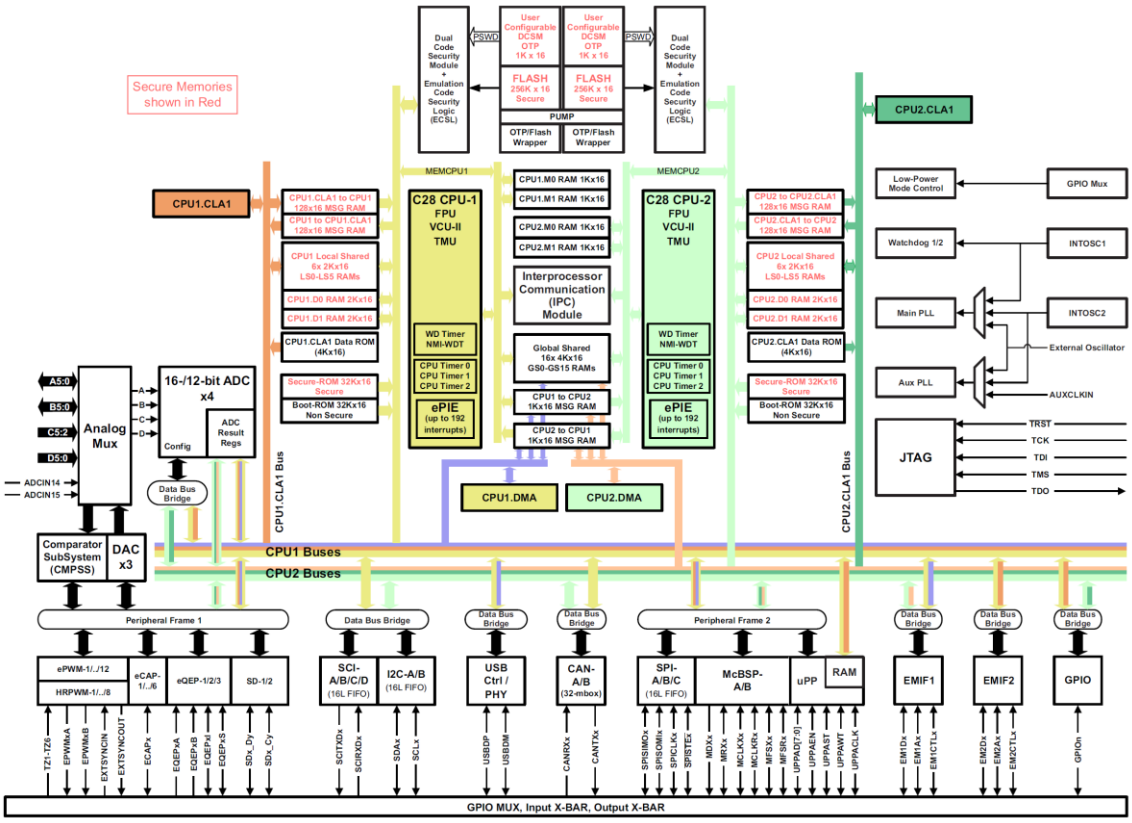

Figure 18: Microcontroller block diagram (Texas Instruments 2015).

3.6 Voltage and Current Measurements

The voltage and current measurements were done using voltage and current transducers. Both transducers are manufactured by LEM.

3.6.1 Current Measurement

The current measurement was done using LEM CASR-6 closed-loop transducer. Some features are listed in Table 5.

Table 5: CASR-6 main features (LEM 2012a)

Feature	Value
Output voltage	0.375 V … 4.625 V
Supply voltage	5 V typical, 7 V maximum
Current measuring range, primary	-20 A…20 A
Current consumption	Depending on the primary current,
Overall Accuracy at 85 °C	1.2 % of primary nominal current
Bandwidth	200 kHz (-1 dB)

As shown in Table 5, the output voltage is close to the maximum voltage that can be applied to the MCU ADC converter. The ADC maximum input voltage is 3.3 VDC, therefore, scaling is required to be done and the scaling is performed using a circuit shown in Figure 19. The circuit includes a first order RC low pass filter due to the fluxgate noise around 450 kHz that was amplified by the amplifier stage. The circuit scales the voltage output from the current transducer to be within acceptable limits of the MCU. The voltage output does not exceed 3 V from the operational amplifier output so it is suitable for the MCU. The measurement of the current transducer circuit is shown in Chapter 4.2.2.

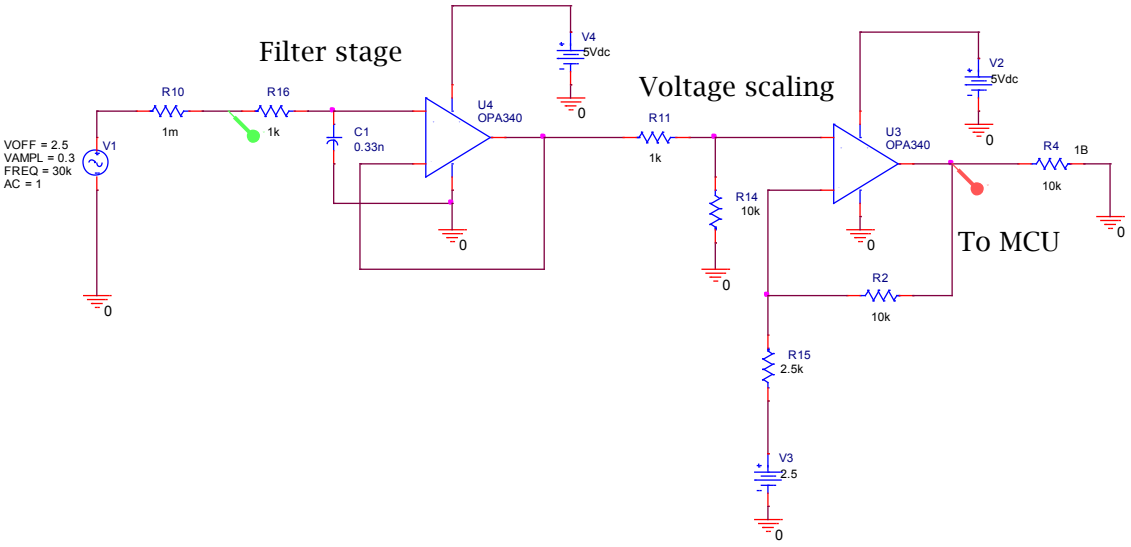

Figure 19: Current transducer circuit.

The simulation was done by assuming 30 kHz frequency and a voltage of 2.5 VDC with 0.3 VAC output swing. The OPA340 model is acquired from Texas Instuments' website. In Figure 20, it is shown how the voltage is scaled for the MCU.

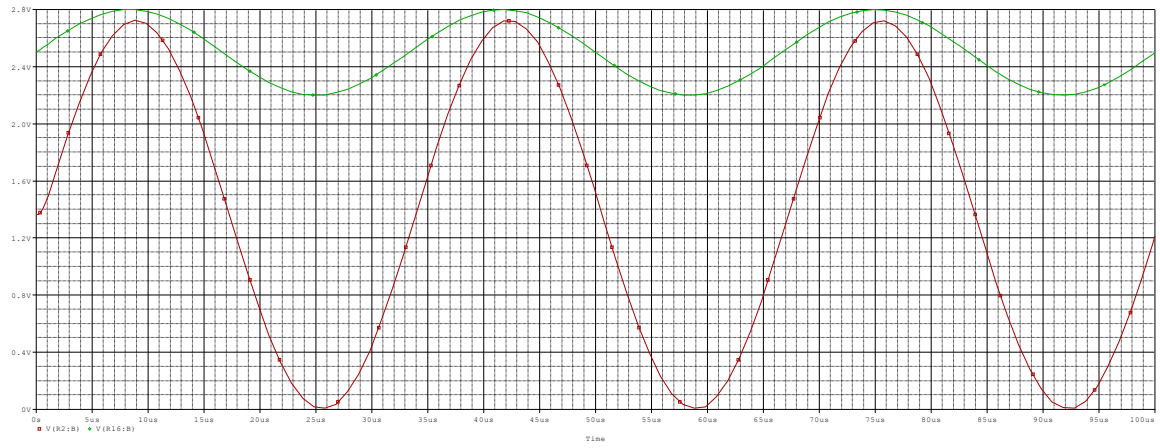

Figure 20: Output voltage of operational amplifier U3, Green = voltage at input, Red = voltage at output. Horizontal scale: 1 µs/div, Vertical Scale: 0.1 V/div. Vmin = 0 V, Vmax = 2.8 V.

3.6.2 Voltage Measurement

Voltage measurement transducer is a closed-loop transducer LV-25P. It requires more designing due to the fact that the transducer uses bipolar supply voltage and thus it cannot be inputted to the ADC converter directly. Some features are listed in Table 6.

Table 6: LV 25-P features (LEM 2012b)

Feature	Value
Supply voltage	± 12 VDC … ± 15 VDC
Output Voltage @ Vss ± 15 V	± 15 VDC
Conversion ratio	2500:1000
Primary nominal current	10 mA
Overall accuracy	0.9 % at primary nominal current

A circuit was modelled to ensure that the output voltage remains in the desired range that is defined by the MCU ADC maximum input voltage of 3 VDC. The circuit is presented in Figure 21.

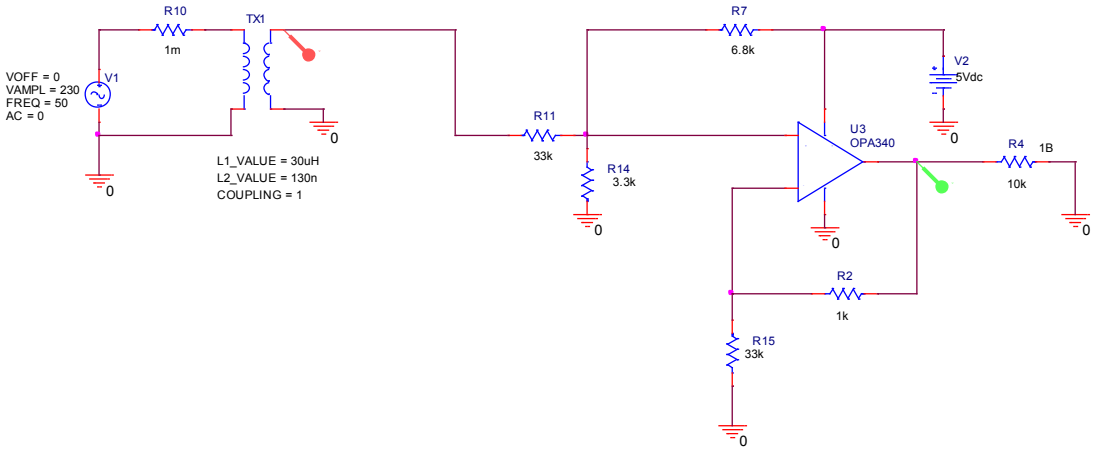

Figure 21: Voltage measurement circuit.

A transformer is used as a voltage transducer model, shown on the left side in Figure 21. The transformer TX1 coil inductances are chosen arbitrarily so that the voltage at the secondary side is similar to the actual output level in order to model the actual voltage transducer. The coupling is set to 1 to let the transformer be ideal. The measurement op amp U3 SPICE model for OPA340 was acquired from the Texas Instruments' website. The OPA340 is a single operational amplifier operating with a single supply. The realization uses OPA4340, which is a quad operational amplifier version of the OPA340. In the figure, R7, R11 and R14 create a voltage divider that sets the output voltage to a suitable level. The signal is then connected to the positive voltage terminal of the opamp so there are no inversion in the output signal. This reduces efforts in software development.

The amplification of the circuit is calculated as follows,

$$V_{OUT,VT} = \left(1 + \frac{R_2}{R_{15}}\right) V_{IN,VT}, \qquad (3\text{-}27)$$

and the input voltage is sinusoidal signal and the results are simulated in Figure 22. The problem in the non-inverting configuration is that the signal cannot be attenuated in the operational amplifier.

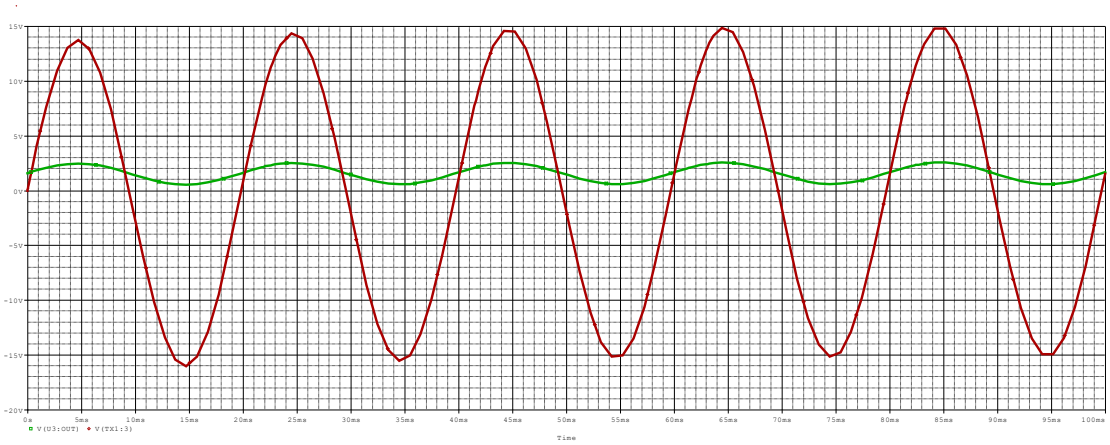

Figure 22: Voltage measurement circuit performance. Green: Opamp output, Red: Voltage transducer output. Horizontal scale: 1 µs/div, Vertical Scale: 1 V/div. Vmin = -20 V, Vmax = 15 V.

As seen in the Figure 22, the output voltage remains in the levels between 590 mV and 2.52 V. This is sufficient amplitude for the MCU ADC. The measurement is done using the cursors that are left out of the figure.

3.7 Thermal Design

Thermal design for the first prototype was not under greater considereration. Thermal design was made with several assumptions and simplifications, due to the fact that the first prototype was a proof-of-concept. The initial idea was to choose components that are easy to use and provide some level of thermal relief for the IGBTs. Heatsink was chosen to be Ohmite R2 series heatsink for the TO-247 package and thermally conductive silicon interface pads 3M 5519 1.0 mm was used as a thermal interface material. Thermal conductivity for the silicon pad 4.9 W/mK for at least 3000 hours.

Thermal design of the prototype converter was not specifically designed or simulated due to the fact that the second prototype could differ significantly compared to the first prototype. If evaluated, thermal properties can be simulated using simulation software. Such simulation programs are Comsol Multiphysics and Ansys Icepak, few to mention. Multiphysics requires Heat Transfer Module to be installed within the software and to simulate the thermal properties, it requires a mechanical model to be imported to the

program. Therefore, it requires a mechanical design which is not done due to the nature of the project.

3.8 Auxiliary Components

This section describes the auxiliary components that are not essential to the prototype realization. However, the components would be essential for the converter if the converter ends up to be in production.

3.8.1 Contactor

The contactor was selected to be ABB's AF38Z-30-00-20. It features three-phase contactor which can be switched on and off by a microcontroller. The rated power is 18.5 kW and the maximum current is 50 A (ABB 2011). The contactor is used by the MCU to connect and disconnect the converter from the mains network whether in controlled or normal situations.

3.8.2 EMI Filter

EMI filter for the converter was chosen to be Schaffner's FN3258-16-44. It is a three-phase filter. The features of the EMI Filter are presented in Table 7.

Table 7: EMI filter features (Schaffner 2015)

Feature	Value
Rated Current @ 50 ℃	16 A
Temperature Range	−25 ℃ … + 100 ℃
Maximum Continuous Operating Voltage	480 VAC
Leakage Current @ 400 VAC/50 Hz	33.0 mA
Overload Capability	4x rated current at switch on. 1.5x rated current at 1.5 min/h

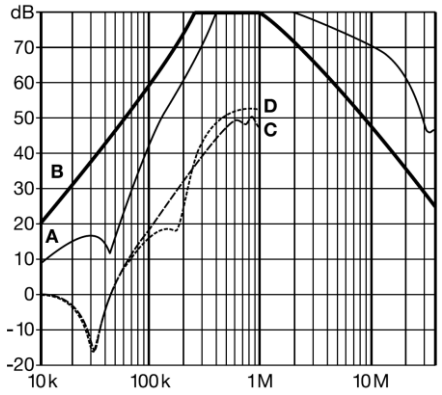

Figure 23: EMI Filter attenuation. (A) 50/50 sym, (B) 50/50 asym, (C) 0.1/100 sym, (D) 100/0.1 sym (Schaffner 2015).

Figure 23 presents the filter attenuation per CISPR17. As seen on the figure, the non-matched load generates bad performance at certain frequencies around 0 Hz to 100 kHz.

4 Realization

This chapter describes the realization of the first converter prototype.

4.1 Resonant Circuit

Since the inductance value is not limited by the application specifically, the inductance value is not accurately defined. The inductance value and the final thickness of the copper wire as well as litz wire were defined by using the $4\,A/mm^2$ to $6\,A/mm^2$ value which is common for copper wires. With a copper wire with 2 mm diameter, the cross section is:

$$\mathbf{A_{wire} = \pi\, r^2 = 3.14\ mm^2} \qquad (4\text{-}1)$$

And using the predefined values of $4\,A/mm^2$ to $6\,A/mm^2$, calculated values are between 12.56 A to 18.84 A when the area of a wire is $3.14\ mm^2$. This is applicable only for low frequencies due to the skin effect. A sophisticated guess for the inductor size was obtained after searching research papers and calculating some guidelines according to Equation (3-1). After obtaining the self-inductance value using a copper wire, an inductor with a self-inductance of approximately 22.7 µH was made. Equation (4-2) was used to determine the resonant frequency of the system.

$$\boldsymbol{f_{RES} = \frac{1}{2\pi\sqrt{22.7\ \mu H * 1\ \mu F}} = 33.4\ kHz} \qquad (4\text{-}2)$$

At this frequency, the RLC impedance is purely resistive and equals to the resistance in the circuit. The simulated circuit is shown in Figure 24 and the impedance of the circuit as a function of frequency is shown in Figure 25. The inductance was verified by using a RLC meter and the capacitor was chosen to be 1 µF. A simulation was performed for the circuit before the realization of the RLC circuit.

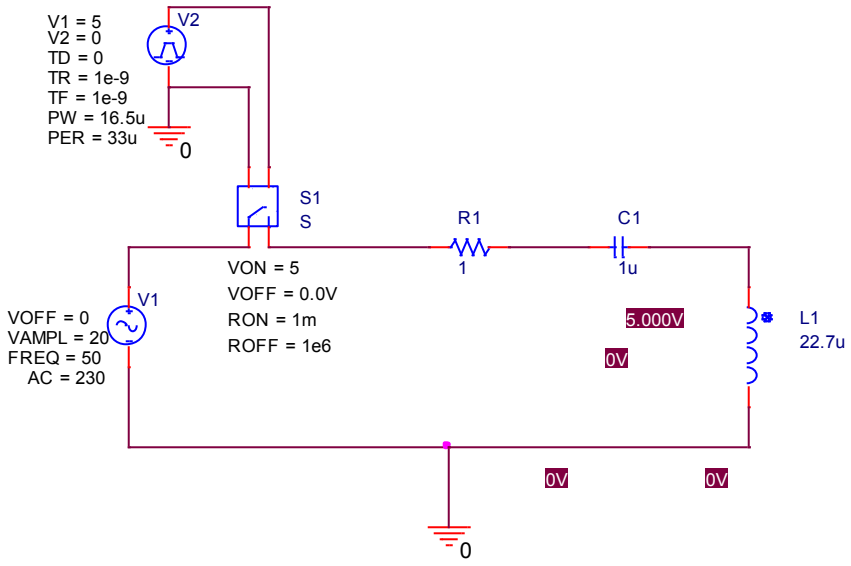

Figure 24: Simulated RLC circuit of the proposed converter.

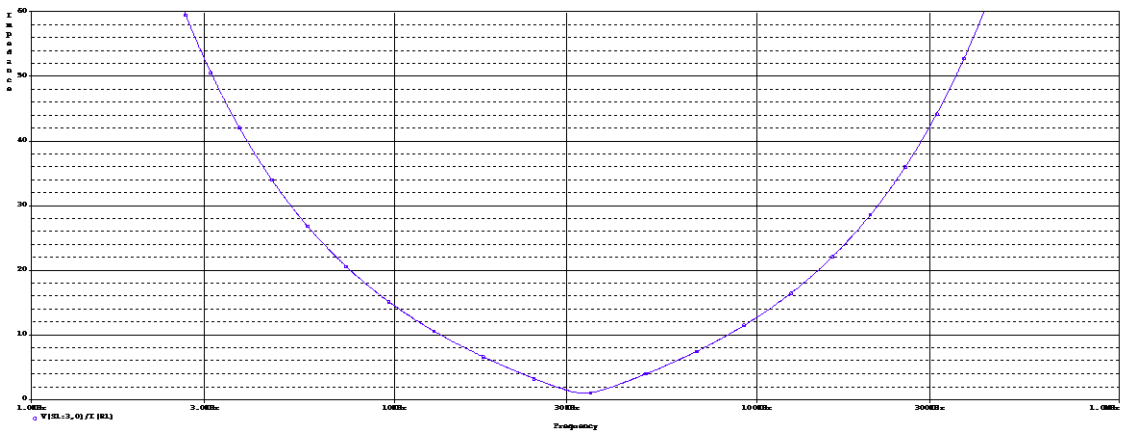

Figure 25: Simulated impedance of the designed RLC circuit.

By using the cursor tool, the frequency is found to be 33.42 kHz when the resistance is 1 Ω. This is very close to the calculated value and the values are used for RLC circuit in the first prototype. The skin effect analysis is neglected in the first prototype due to the difficulties to obtain litz wire and the use of solid copper wire. The RLC circuit is shown in Figure 26.

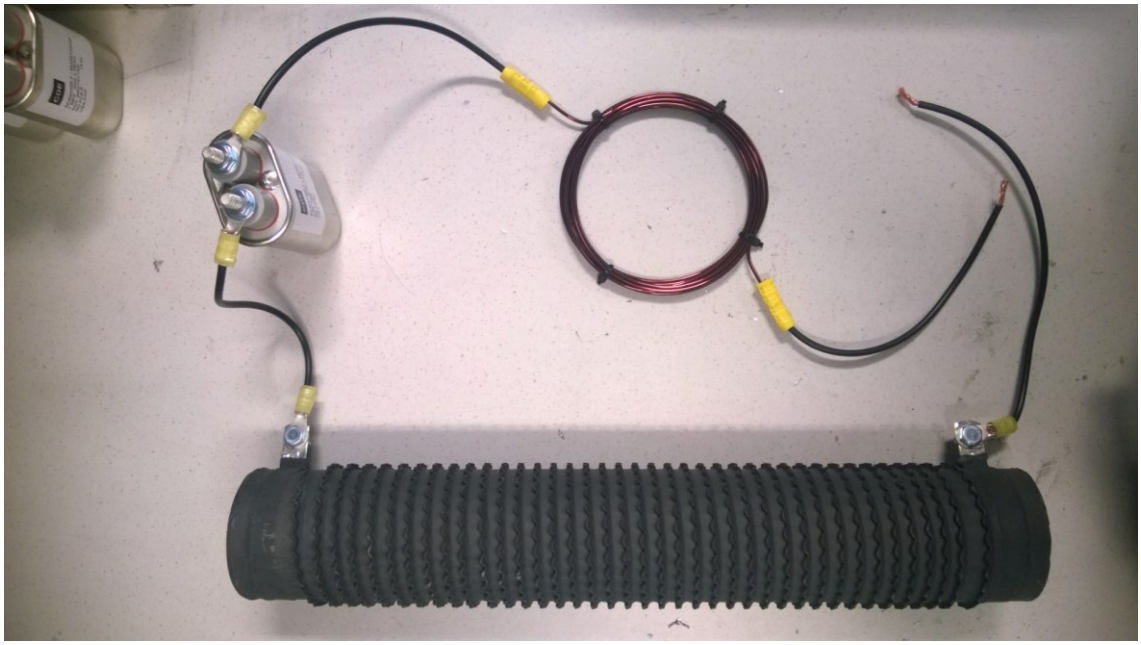

Figure 26: First RLC prototype.

The first prototype estimation of the RLC circuit was designed while keeping in mind that there will be no high current requirements. The cabling between the components is such that it is not suitable for currents above 10 A. The inductance and power losses that it generates are such that it may alter systems' overall performance. The testing phase shows the behavior of the resonant circuit.

4.2 Measurement Circuits

As previously mentioned, the measurement sensors provide output voltages that were not possible to be delivered to the MCU directly and they require scaling circuits. The operational amplifiers of the measurement sensors were not placed on the main PCB unit since there was a concern over interferences that the converter may cause which leads to more significant measurement errors due to noise.

4.2.1 Voltage Measurement Circuit

The voltage divider was built using TI's Universal Operational Amplifier Evaluation Module OPAMPEVM-SOIC which is a readymade PCB for various different operational amplifier circuit arrangements. The circuit shown in Figure 21 was built on the PCB for each input phases and connected using prototyping wires.

4.2.2 Current Measurement Circuit

Current transducer circuit was also done using TI's Universal Operational Amplifier Evaluation Module OPAMPEVM-SOIC prototyping board according to the circuit shown

in Figure 19. After building the circuit, the circuitry was tested by inputting sinusoidal currents through the sensor and measuring the output of the opamp U3 of Figure 19. Measurement result is shown in Figure 27.

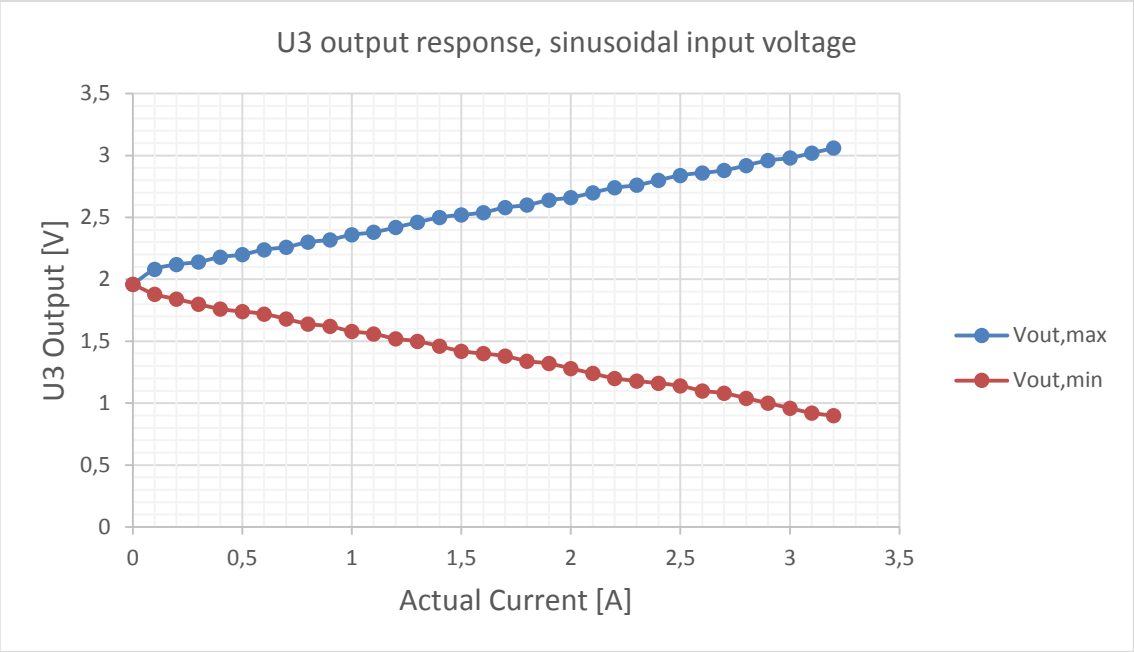

Figure 27: Output voltage of operational amplifier U3 of Figure 19. The figure presents an output range at a certain sinusoidal current. Measurements were done with 100 mA steps. Current was inputted through a resistor and then measurement was done by measuring from the operational amplifier output using oscilloscope.

Measurement of the voltage was done using the measurement function in the oscilloscope. The oscilloscope measurement function is not very accurate to use in measuring the voltages, but since all of the measurements were done with the same oscilloscope, the error is the same for all, resulting a consistent result. The current was verified using a digital multimeter. From the measurement result, it can be seen that at 0 V the output was 1.96 V and the second finding was that 100 mA current produces a 20 mV difference in measured signal.

4.3 Schematics

The schematics of the converter prototype were drawn using OrCAD. The schematics design includes all components drawn according to the manufacturer datasheets and specifications. It is presented in Appendix A.

4.4 PCB

A printed circuit board was created for the first prototype in order to test the topology idea. The PCB was ordered from Prinel Oy, Tuusula. The PCB order was provided with Gerber files and sent to the supplier along with the PCB specification. The PCB layout is presented in Appendix B.

4.4.1 PCB Specification

In order to give specification for the PCB, various sources were studied. The reason for this is that with higher current requirement, the thermal phenomena is an increasing concern. The final source of choice as a guide line for the specification was considered to be from Semikron's application note AN1402 for PCB design of MiniSKiiP dual devices. The main features of the PCB is presented in Table 8 below. (Staudt 2014)

Table 8: PCB Specification

Feature	Value
Layers	4
Thickness	2.0 mm
Finish	Ag
Solder Mask	Green
Copper thickness	105 µm

The Semikron's application note shows that the PCB worked well with above 100 A current. Due to the character of the project, no complete specification document were done for the project and the PCB order included the PCB specification in an e-mail to the supplier.

4.5 Complete prototype

A complete assembled board is presented in Figure 28. The prototype was manually assembled by soldering the components in place in the machine hall of Aalto University School of Electrical Engineering and Automation.

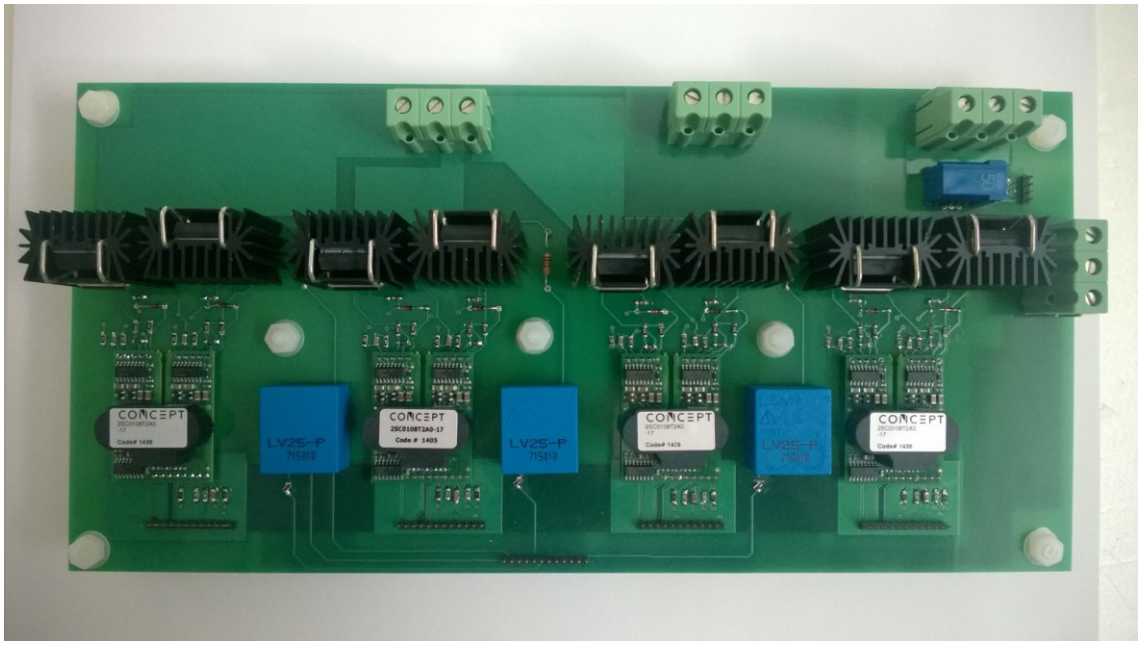

Figure 28: First PCB prototype.

The switches are shown on the middle with the heat sinks (black components). The IGBT drivers (Concept labels) are shown below the switches and the voltage sensors are shown next to the IGBT drivers (blue squares). Current sensor (blue rectangular) is shown in the upper right corner next to the 3 pole connectors (green blocks).

4.6 Microcontroller and Software

The software for the MCU was done with Texas Instruments' Code Composer Studio. The program's flow chart is shown in Figure 29. This shows the main idea for the switching in the converter. The MCU of the converter was assembled in the prototyping box. For prototyping reasons, a keypad and a display was added to the prototype in order to manually check and adjust parameters during the operation. The keyboard was a 12 button keypad with an asterisk and a hash key.

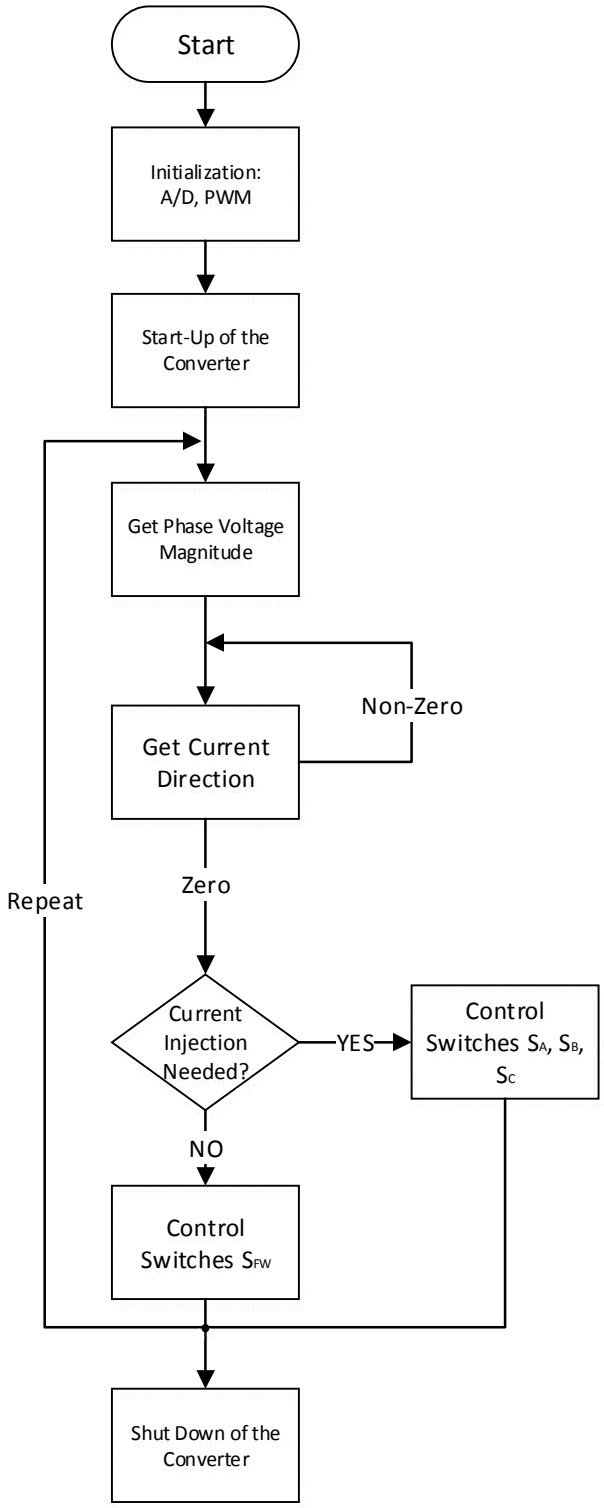

Figure 29: The converter control software flowchart.

The software starts by initializing the required functionality such as ADC, PWM timers and dual core CPU communications. After the initializations, it measures the phase voltage absolute values to determine which phase will be used to inject energy into the

load. This also requires the current direction to be seen in order to control the switches. The need of the current injection comes from the load side which is not part of the project but for the testing, it is set to always needed. This means that the converter operates at the maximum output power at all cases. In later phases of testing, the secondary side will be tested with the converter.

5 Testing

This chapter describes the testing of the functionality of the converter.

5.1 Functional Testing of Power Supply

Usually, the testing of a complete converter is done in such a manner that the operation is verified against the product specification. In this case, the design input is the product specification from the design team. The functional test is generally more comprehensive than production testing which tests only if the feature is working or not working. The quality of the test result is defined during the functional testing. The functional testing is usually carried out by the product design team. (Crandall 1997)

The test plan for the power supply consists of test steps that can be divided into several categories:

- AC input tests
- DC input tests
- AC output tests
- DC output tests
- Control input tests
- Ancillary output tests

Each power supply is also tested accordingly for electromagnetic compatibility at the certified test laboratory to ensure that the converter may be labeled with the CE mark. More detailed description of the testing can be found from APPENDIX C.

5.2 Testing of the converter

As shown in this thesis, the most critical testing issue is to verify that there is no short circuit between the phases or from phase to PE. These can occur if the timing of gate driving signals is not correctly designed. The issue is handled in the software but the lack of knowledge of the overall inductance in the circuit is creating an uncertainty if the circuit commutation creates a risk of short circuit. The testing was started by testing the short circuits on the PCB after assembling all the components. The timings of the gate drivers were measured after the initial tests so that they were not short circuiting the phase to PE through the phase switch to free-wheeling switch. In Figure 30, it is shown that the switching employs a dead time between the gate signals. The figure presents only the phase A, since all the phases showed similar behavior. The dead time

was designed to be at least 20 µs and this criteria was met, which is shown in Figure 31. All gate signals are showing the same behavior so only one phase is shown.

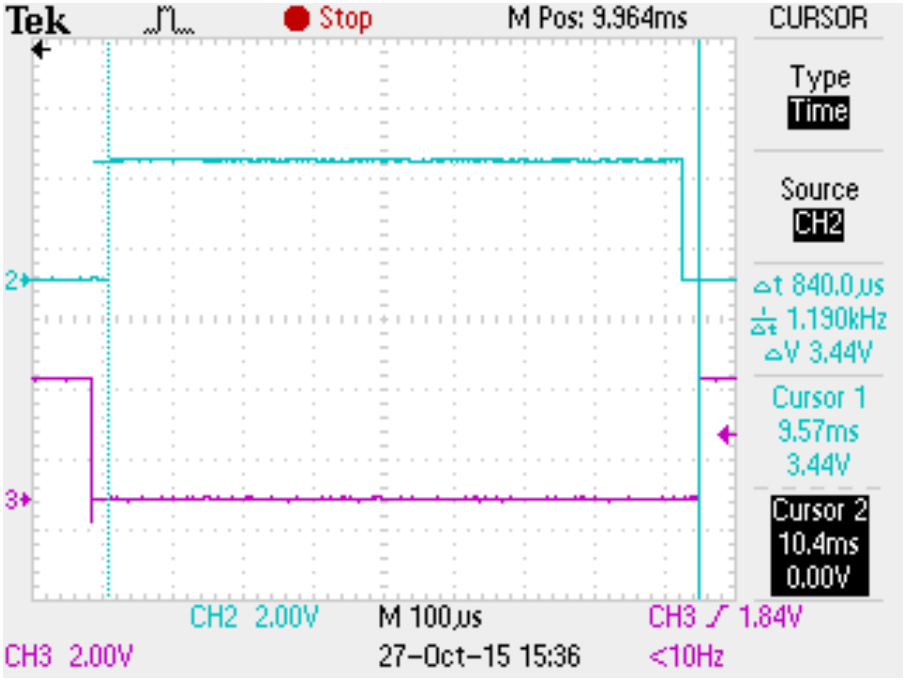

Figure 30: Dead-time shown with clear gaps between the gate drive signals. Ch2, blue: Freewheeling switch, Ch3, red: Phase a positive switch.

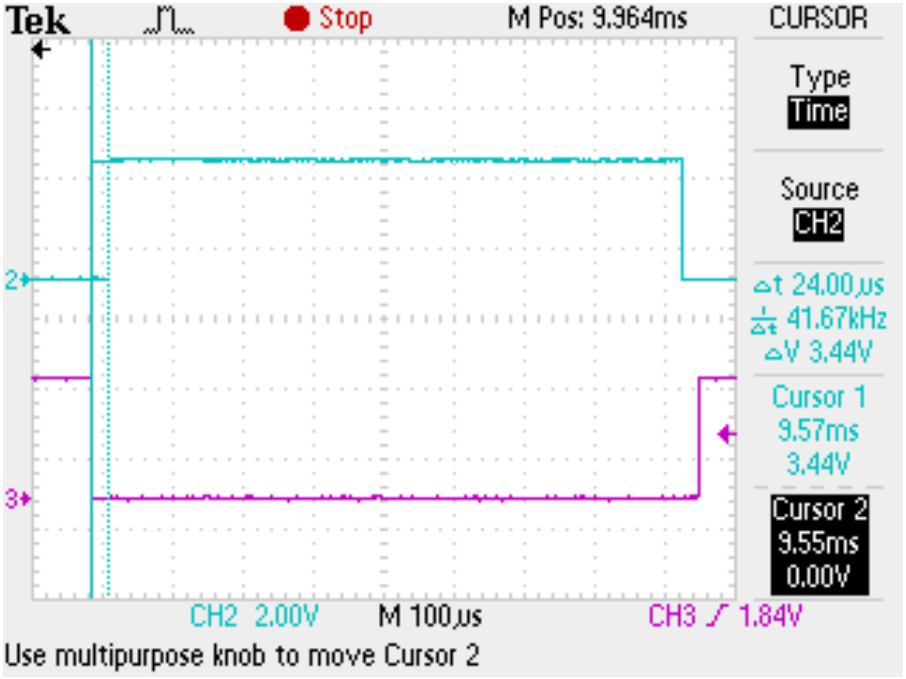

Figure 31: Figure shows the dead-time of 24 µs between the gate signals. Ch2, blue: Freewheeling switch, Ch3, red: Phase a positive switch.

Figure 32 and Figure 33 shows the output of the voltage transducer opamps and Figure 34 shows the output of the current transducer opamp. These signals are delivered to the MCU ADC.

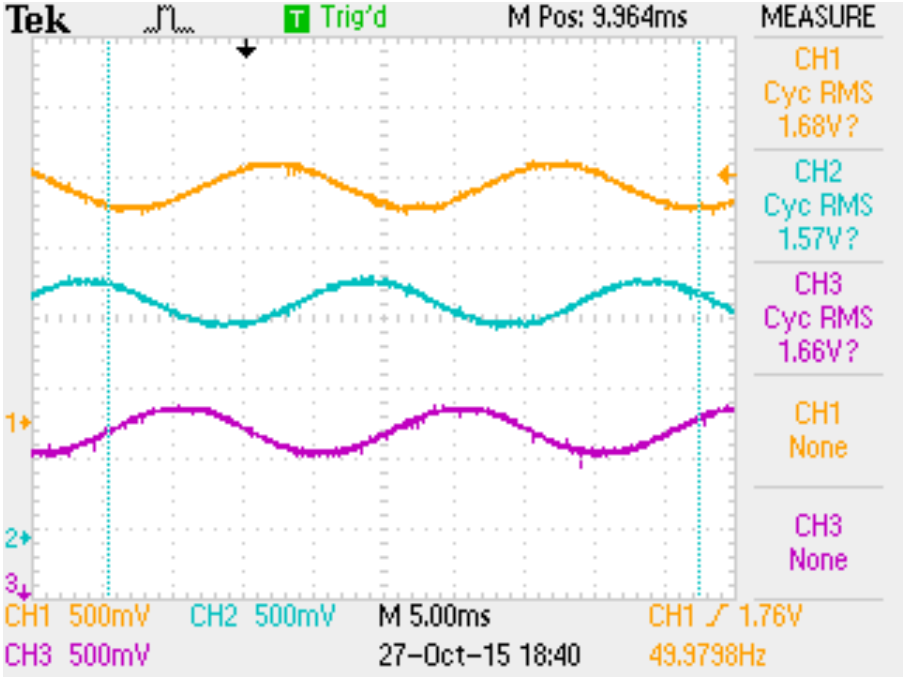

Figure 32: Output signals of the voltage measurement operational amplifiers. The converter is inputted with 20 VAC and the voltage is measured with the voltage measurement transducers. The signal is then scaled with operational amplifier circuits and delivered to the MCU ADC. These signals show that the voltage levels are suitable (between 0 V to 3.3 V) and the signals are low noise. The right hand side of the figure shows the measured RMS voltage.

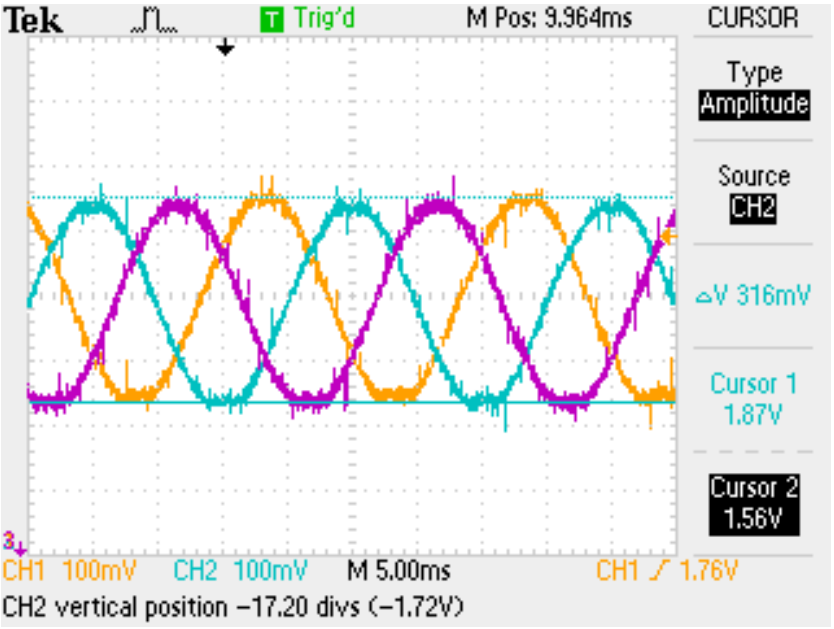

Figure 33: Output signals of the voltage measurement operational amplifiers. This figure shows three-phase voltage amplitude of 316 mV on the right hand side of the figure when input voltage is 20 VAC. DC level is 1.715 VDC.

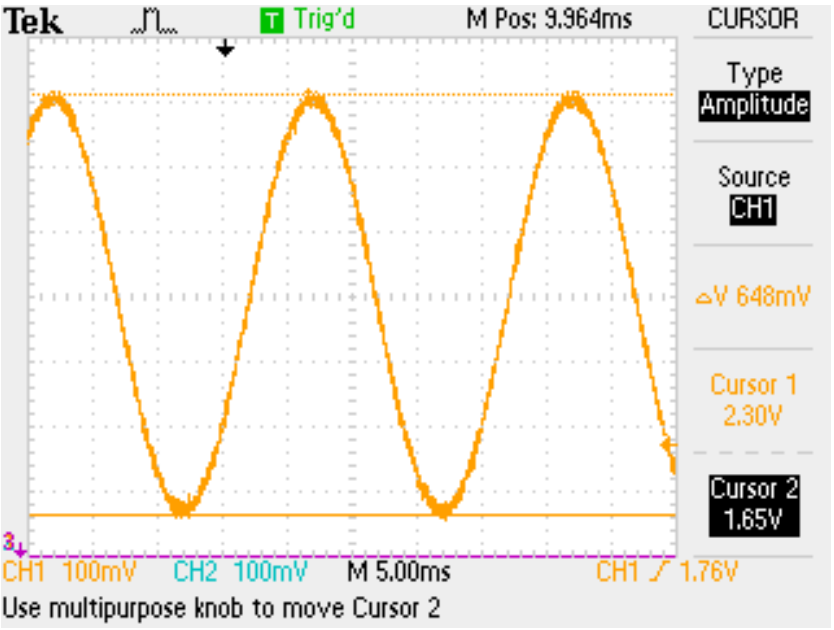

Figure 34: Output signal from the operational amplifier circuit of the current transducer when the current is 1 A. The current is verified by using a digital multimeter. The voltage swing is shown on the right hand side of the figure and its peak-to-peak value is 648 mV. DC level is 1.975 VDC.

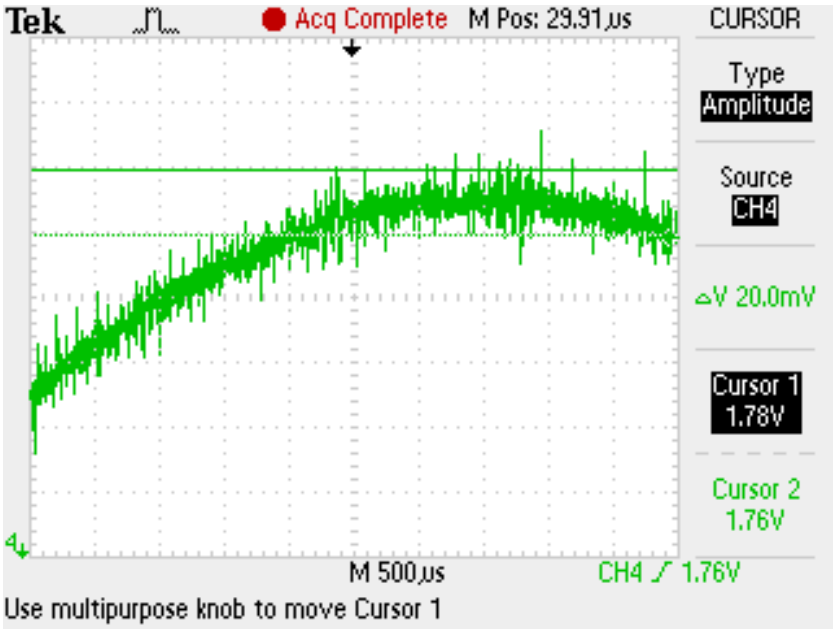

Figure 35: Averaged noise of the voltage measurement transducer operational amplifier. Noise voltage is approximately 20 mV with oscilloscope probe noise. Input voltage is 20 VAC.

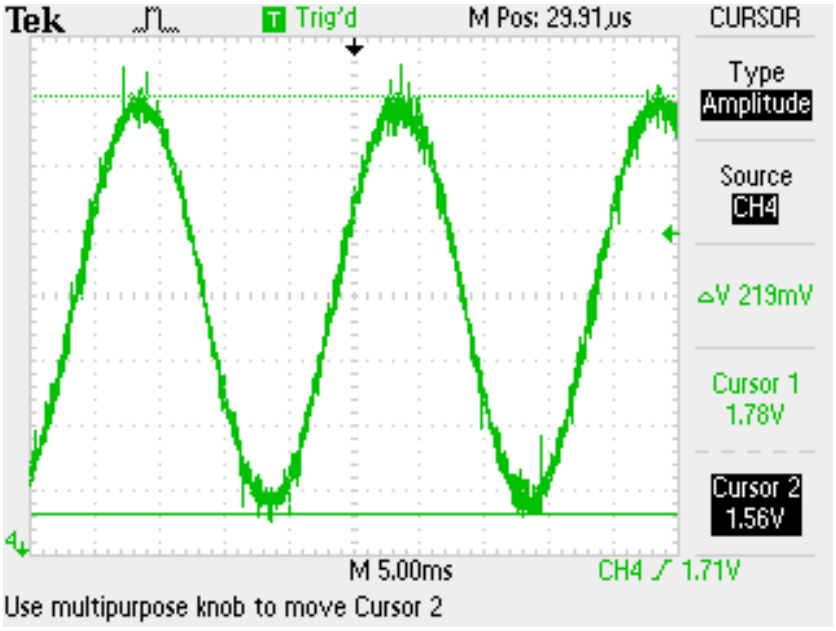

Figure 36: Measured phase voltage from operational amplifier output. The amplitude of the voltage is approximately 220 mV when the input is 20 VAC. The ratio of the noise to measured voltage is 9.09 % which is significant.

The oscilloscope probe noise is measured to find out the level of noise in the measurement equipment. Figure 37 shows the used probe and Figure 38 shows the measurement result.

Figure 37: Measurement of probe noise.

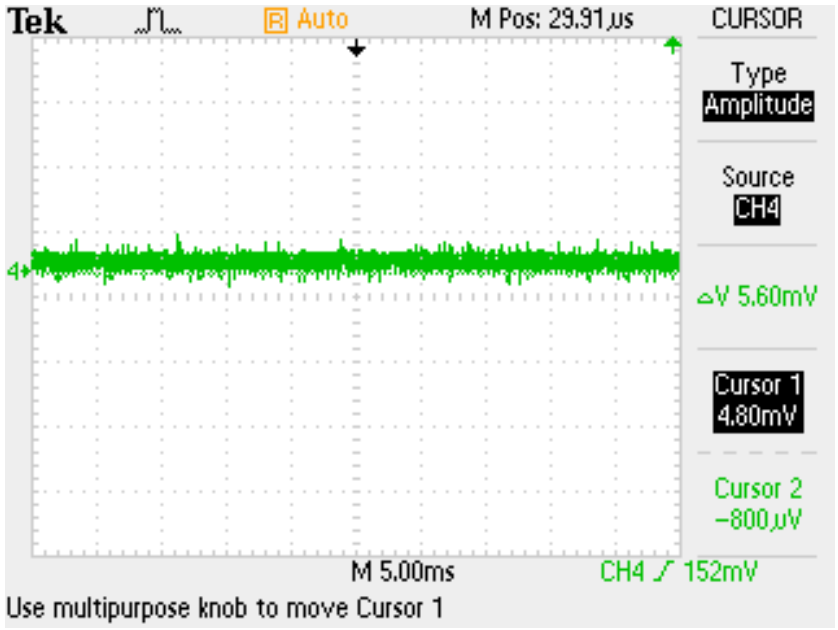

Figure 38: Measured probe noise. The noise voltage level is 5.6 mV. This voltage is subtracted from the measured phase voltage.

Therefore, the measurement has approximately 15 mV of actual noise in the signal which reduces the noise in the signal to approximately 6.8 %, which is still too much. The noise effect would be smaller if the input voltage amplitude is increased.

5.2.1 Test Equipment

Following test equipment was used:

- Three channel laboratory DC supply GW Instek SPD-3606
- Three-phase laboratory AC supply Elgar SW5250A
- Digital multimeters Fluke CNX3000 and Fluke 28II
- Oscilloscope Tektronix TPS2014B
    - Differential probes, galvanically isolated Tektronix P5200A
    - Passive probes Tektronix 10X
    - Current probes Tektronix A622
- IR camera Fluke thermal imager

6 Conclusion

The realization of the direct AC/AC converter was presented. The initial idea was to make a converter that is suitable for high power applications, but in the making of the converter, lower power version was decided to be done as a first prototype. The next chapter, Future Work, presents the discussion about the second prototype which is going to be designed for the project.

The proposed converter was designed using the IGBTs as switching components but during the project, it became clear that next prototype should use SiC MOSFET components due to the improved efficiency and increased switching frequency. When increasing the switching frequency, the driver circuitry needs to be designed for the higher switching frequency. The driver in this project supports switching frequency up to 50 kHz, which means that it will probably be obsolete for the next prototype.

The heatsink and the silicone thermal interface material were found out to be great for the prototyping purposes but their performance is not enough. The idea was to use any thermal interface just to speed up the practical realization task and this found out to be unsuccessful method to create a successful thermal design. After the design of the first prototype, it was noticed that the heatsink should be significantly bigger than initially designed when a higher power version is required.

The measurement circuits were not good enough to work with this kind of project. Therefore, a fully differential measurement with better cabling is required. The idea was to use hysteresis in the software but it turned out to be inadequate solution for this. Therefore, next chapter discusses the new solution for this. The reason for opamps to be at their own PCBs was to reduce the risk of possible EMI that the converter produces. The cabling was thought to be “good enough” with regular copper wires.

However, the biggest challenge in this project was the complexity of the software. The software did not operate as required within a reasonable time frame. Software development should be started earlier in such projects, while in this, it was started only after 2 months after the project started.

Some ideas could not be tested such as connecting the converter to mains network. Thus, the operation of the converter while connected to mains network is not known. Up to the point when this thesis was finished, only a three-phase laboratory supply were used. This unfortunately means that there is no data on how this converter affects the mains network. The idea was that the power factor should be high due to the sinusoidal current

drawn from the mains and the converter produces less losses. However, the EMI caused by the switching, should be studied in later phases of the forthcoming research.

In the future, this project can be used as a basis for a new thesis/project and the project should fix all the problems that were found during this thesis project work. The future project should focus on the resonant circuit study and improvements of the transmitting circuit when the secondary is added. One particularly interesting study might be the usage of the proposed converter in resonant converters such as LLC converters. This might be realized when the transmitting circuit is changed to transformer which forms the resonant circuit.

6.1 Testing Conclusions

The hardware prototype was manufactured in the early stages of the project and the following features were briefly tested:

- Current measurement
- Voltage measurement
- Gate drivers
- IGBTs

There were manually built parts in order to get the converter working. Before testing the converter with the MCU, the hardware was assumed to be working as it should. However, there was some changes due to the findings in the testing. The V_{CE} de-saturation protection was disabled for AC reasons. Later developments should address this by studying the use of a diode in the V_{CE} de-saturation protection.

Chapter 7 discusses proposed actions to build a working prototype that is based on the findings during the testing of the converter.

7 Future Work

Future work of the converter should focus on these features:

- Measurement accuracy
- SiC MOSFET switches and their driving circuit
- Wireless power transmitter circuit
- Power component design
- Mechanical design of the converter

The next design phase of this converter is planned to be the converter using SiC MOSFET components that enable higher switching frequency while providing more power with better efficiency. The driving method of the SiC MOSFET switches should be similar to the IGBT's.

One additional problem noticed was that the accurate measurement of the three-phase voltages and the load current requires better noise performance. The problem was found out to be the operational amplifier circuits and the cabling between the circuits. One possible solution is to use a fully differential operational amplifier and add coaxial cables for interconnecting the parts. One such type could be THS4531A, which has an evaluation module available widely on the markets. This enables removing the interference from the measured signal. The measurement signal cabling should be also reconsidered and coaxial cables should be used to transmit the measured signal. There were significant amount of issues when the current and voltage were measured using only single-ended operational amplifier.

Figure 39 presents one possible configuration for the second prototype and the build was found out to be the most suitable according to research papers. The design is based on stacking the PCBs on top of each other including the control PCB, measuring PCB and switch board. The switch board depends on the switching component type and is needed if PCB assembled components, such as TO247, are used. The TI control card is connected to a control board using an appropriate connector for its connection. This also reduces the cabling distances between the boards. The top PCB also includes the power connector for the control card and measurement circuits. The middle PCB is populated with the measurement transducers and the switch drivers as well as additional circuits that are required by the drivers and sensors to operate.

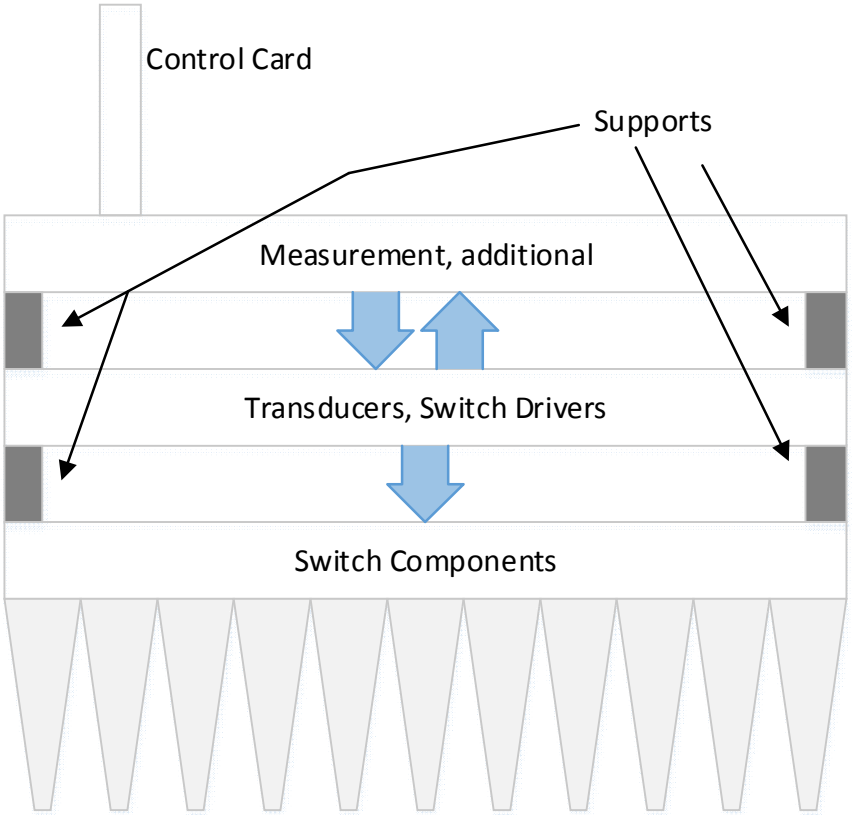

Figure 39: Recommended build for the next prototype.

Blue arrows designate the direction of information between the boards. When designing the cabling, one must also take into consideration that there are significant amount of EMI around the converter which means that the cabling must be well designed as well as the cabling order for the wires must be considered carefully.

The wireless power transmitter circuit requires also a better study on how to make it to achieve optimum efficiency for the transmitter. From a hardware point of view, the coil needs to be built using a litz wire (If the calculations shows that it is needed) and the best possible core material should be selected for it. Round shape coil seems to be the best option due to the flux alignment.

Thermal design needs to be improved from the first prototype. The first prototype was designed to ensure that the idea is working, so the high power transferability was not included. This means that the heatsink needs to be calculated according to the switches that dominate the energy losses during the switching. If the heat calculations show that passive cooling is not adequate, fans should be attached to the one end of the heat sink to obtain forced cooling and better thermal performance.

Bibliography

1. ABB 2011, , ***Datasheet: AF38-30-00-.. / AF38Z-30-00-.. 3-pole Contactors AC / DC Operated - with Screw Terminals***. Available: https://library.e.abb.com/public/be564d4ae0c70b8fc1257861003881db/1SBC101412D0201.pdf [2015, 08/20].

2. Abjihit, D.P. & Locher, R.E. 2009, , ***Application note: IXAN0009, HOW TO DRIVE MOSFETs AND IGBTs INTO THE 21ST CENTURY*** [Homepage of Ixys Corporation], [Online]. Available: http://www.ixys.com/documents/appnotes/ixan0009.pdf [2015, 25/08].

3. Bosshard, R., Kolar, J.W., Muhlethaler, J., Stevanovic, I., Wunsch, B. & Canales, F. 2015, "**Modeling and --Pareto Optimization of Inductive Power Transfer Coils for Electric Vehicles**", *IEEE Journal of Emerging and Selected Topics in Power Electronics,* [Online], vol. 3, no. 1, pp. 16.09.2015. Available from: http://ieeexplore.ieee.org/stamp/stamp.jsp?tp=&arnumber=6762832.

4. Casadei, D., Serra, G., Tani, A. & Zarri, L. 2002, "**Matrix converter modulation strategies: a new general approach based on space-vector representation of the switch state**", [Online], vol. 49, no. 2, pp. 8.6.2015. Available from: http://ieeexplore.ieee.org/stamp/stamp.jsp?tp=&arnumber=993270.

5. CDE 2015, , ***Datasheet: Type SF Motor-Run and Power Supply Capacitors*** [Homepage of CDE], [Online]. Available: http://www.cde.com/resources/catalogs/SF.pdf [2015, 08/18].

6. Cornell Dubilier 2015, ***E-mail: Thermal Resistance of SF Capacitor***.

7. Crandall, E. 1997, ***Power Supply Testing Handbook: Strategic Approaches in Test Cost Reduction,*** Chapman & Hall, USA.

8. Empiringham, L., Kolar, J.W., Rodriguez, J., Wheeler, P. & Clare, J.C. 2013, "**Technological Issues and Industrial Application of Matrix Converters: A Review**", [Online], vol. 60, no. 10, pp. 8.6.2015. Available from: http://ieeexplore.ieee.org/stamp/stamp.jsp?tp=&arnumber=6290364.

9. Gangyao, W., Fei, W., Magai, G., Yang, L., Huang, A. & Das, M. 2013, "**Performance comparison of 1200V 100A SiC MOSFET and 1200V 100A silicon IGBT**", *Energy Conversion Congress and Exposition (ECCE), 2013 IEEE,* [Online], , pp. 11.08.2015- DOI: 10.1109/ECCE.2013.6647124. Available from: http://ieeexplore.ieee.org/stamp/stamp.jsp?tp=&arnumber=6647124.

10. Graovac, D. & Pürschel, M. 2009, "**IGBT Power Losses Calculation Using the Data-Sheet Parameters**", [Online], , pp. 11.08.2015. Available from: https://www.google.fi/url?sa=t&rct=j&q=&esrc=s&source=web&cd=2&ved=0CCsQFjABahUKEwjt_Yma4J7HAhWkqHIKHWl0DkI&url=https%3A%2F%2Fwww.element14.com%2Fcommunity%2Fservlet%2FJiveServlet%2Fdownload%2F20553-1-3493%2FIGBT%2520Power%2520Losses%2520Calculation%2520using%2520the%2520Data%2520Sheet%2520Parameters.pdf&ei=objIVa2pL6TRygPp6LmQBA&usg=AFQjCNGZtiAk6Ode30vwCYk81AnXbTcNVw&bvm=bv.99804247,d.bGQ&cad=rja. [11.08.2015].

11. Hazra, S., De, A., Cheng, L., Palmour, J., Schupbach, M., Hull, B., Allen, S. & Bhattacharya, S. 2015, "**High Switching Performance of 1700V, 50A SiC Power MOSFET over Si IGBT/BiMOSFET for Advanced Power Conversion Applications**", *Power Electronics, IEEE Transactions on (Volume:PP , Issue: 99),* [Online], vol. PP, no. 99, pp. 11.08.2015. Available from: http://ieeexplore.ieee.org/stamp/stamp.jsp?tp=&arnumber=7105923&tag=1. [11.08.2015].

12. Hui, S.Y.R., Wenxing, Z. & Lee, C.K. 2014, "**A Critical Review of Recent Progress in Mid-Range Wireless Power Transfer**", *Power Electronics, IEEE Transactions on (Volume:29 , Issue: 9),* [Online], vol. 29, no. 9, pp. 13.08.2015. Available from: http://ieeexplore.ieee.org/stamp/stamp.jsp?tp=&arnumber=6472081&tag=1.

13. Imura, T. & Hori, Y. 2011, "**Maximizing Air Gap and Efficiency of Magnetic Resonant Coupling for Wireless Power Transfer Using Equivalent Circuit and Neumann Formula**", *IEEE Transactions on Industrial Electronics,* [Online], vol. 58, no. 10, pp. 27.08.2015. Available from: http://ieeexplore.ieee.org/stamp/stamp.jsp?tp=&arnumber=5709980.

14. Infineon 2015, 2015-01-26-last update, ***Datasheet:
IHW40N120R3 Reverse Conducting IGBT with monolithic body diode***. Available: http://www.infineon.com/dgdl/Infineon-IHW40N120R3-DS-v02_02-EN.pdf?fileId=db3a30433a047ba0013a6e8aa8405fe2 [2015, 08/10].

15. Jaegue, S., Seungyong, S., Yangsu, K., Seungyoung, A., Seokhwan, L., Guho, J., Seong-Jeub, J. & Dong-Ho, C. 2013, "**Design and Implementation of Shaped Magnetic-Resonance-Based Wireless Power Transfer System for Roadway-Powered Moving Electric Vehicles**", *Industrial Electronics, IEEE Transactions on,* [Online], vol. 61, no. 3, pp. 24.08.2015. Available from: http://ieeexplore.ieee.org/stamp/stamp.jsp?tp=&arnumber=6502703.

16. Kazimierczuk, M.K. (ed) 2014, ***High-frequency magnetic components***, 2nd edn, Wiley Blackwell, Chichester, West Sussex.

17. Kolar, J.W., Friedli, T., Rodriguez, J. & Wheeler, P. 2011, "**Review of Three-Phase PWM AC–AC Converter Topologies**", [Online], vol. 58, no. 11, pp. 8.6.2015. Available from: http://ieeexplore.ieee.org/stamp/stamp.jsp?tp=&arnumber=5873144.

18. Kusumah, F., Vuorsalo, S. & Kyyrä, J. 2015, "**A Direct Three-Phase to Single-Phase AC/AC Converter for Contactless Electric Vehicle Charger**", [Online], , pp. 10.08.2015. [10.08.2015].

19. LEM, C.T. 2012a, 8.3.2012-last update, ***Current Transducer CASR series***. Available: http://www.lem.com/docs/products/casr%20series.pdf [2015, 08/03].

20. LEM, V.T. 2012b, 20.12.2012-last update, ***Datasheet, Voltage Transducer LV-25P***. Available: http://www.lem.com/docs/products/lv%2025-p.pdf [2015, 08/03].

21. Mizuno, T., Ueda, T., Yachi, S., Ohtomo, R. & Goto, Y. 2012, "**Efficiency dependence on wire type for wireless power transfer of magnetic resonant coupling**", *15th International Conference on Electrical Machines and Systems (ICEMS), 2012,* [Online], , pp. 17.08.2015. Available from: http://ieeexplore.ieee.org/stamp/stamp.jsp?tp=&arnumber=6401783.

22. Niiranen, J. (ed) 2007, ***Tehoelektroniikan Komponentit***, 4th edn, Otatieto Helsinki University Press, Helsinki.

23. Nissan 2011, , ***"LEAF to home" Electricity Supply System***. Available: http://www.nissan-global.com/EN/TECHNOLOGY/OVERVIEW/leaf_to_home.html [2015, 08/20].

24. Ohmite 2015, , ***Datasheet: Ohmite R2 series***. Available: http://www.ohmite.com/cat/sink_r2.pdf [2015, 08/11].

25. Schaffner 2015, , ***Datasheet: 3-Phase Filters FN 3258***. Available: schaffner.com/en/products/datasheet-low-res/product/fn-3258-ultra-compact-emcemi-filter-for-3-phase-systems-and-motor-drives.pdf [2015, 08/18].

26. Schulz, M. 2014, "**Thermal Management Details and their Influence on the Aging of Power Semiconductors**", *Power Electronics and Applications (EPE'14-ECCE Europe), 2014 16th European Conference on,* [Online], , pp. 02.09.2015. Available from: http://ieeexplore.ieee.org/stamp/stamp.jsp?arnumber=6910898.

27. Schulz, M. 2013, "**Designed to last - electrical and thermal aspects in power electronic designs**", *Industrial Technology (ICIT), 2013 IEEE International Conference on,* [Online], , pp. 28.08.2015. Available from: http://ieeexplore.ieee.org/stamp/stamp.jsp?tp=&arnumber=6505722.

28. Schweizer 2015, , ***p² Pack the Power Embedding Solution***. Available: http://www.schweizer.ag/en/products-solutions/embedding/p2_Pack_en.html [2015, 09/02].

29. Staudt, B. 2014, 19.12.2014-last update, ***AN1402 - MiniSKiiP Dual – Utilization, PCB Design Recommendations and Test Results*** [Homepage of Semikron], [Online]. Available: http://www.semikron.com/dl/service-support/downloads/download/semikron-application-note-an-1402-miniskiip-dual-en [2015, 07/27].

30. Szczesniak, P. (ed) 2013, ***Three-Phase AC-AC Power Converters Based on Matrix Converter Topology***, 1st edn, Springer -Verlag, London.

31. Tesla, N. 1914, ***Apparatus for transmitting electrical energy***, US1119732 A edn, US.

32. Texas Instruments 2015, , ***Datasheet: TMS320F2837xD Dual-Core Delfino™ Microcontrollers***. Available: http://www.ti.com/lit/ds/symlink/tms320f28377d.pdf [2015, 12.08.2015].

33. Van den Bossche, A. & Valchev, V.C. (eds) 2005, ***Inductors and Transformers for Power Electronics***, CRC Press, Boca Raton, FL.

34. WiTricity 2015, , ***WiT-3300***. Available: http://witricity.com/products/wit-3300/ [2015, 08/13].

35. Ziogas, P.D., Khan, S.I. & Rashid, M.H. 1986, "**Analysis and Design of Forced Commutated Cycloconverter Structures with Improved Transfer Characteristics**", [Online], vol. IE-33, no. 3, pp. 8.6.2015. Available from: http://ieeexplore.ieee.org/stamp/stamp.jsp?tp=&arnumber=4158732&tag=1.

Appendix A - Schematics

REVISION RECORD			
LTR	ECO NO:	APPROVED:	DATE:

HS1 HSINK
HS2 HSINK
HS3 HSINK
HS4 HSINK
HS5 HSINK
HS6 HSINK
HS7 HSINK
HS8 HSINK

INPUT CONNECTOR
J2 CONN_3PIN

GROUND CONNECTOR
J8 CONN_3PIN

LOAD CONNECTOR
J7 CONN_3PIN
J9 CONN_3PIN

Q9 LV25-P (R14, R17)
Q7 LV25-P (R13, R16)
Q8 LV25-P (R15, R18)
J5 CONN_12PIN

U2 25C0108T
J3 CONN_12PIN (R22, R21)
R19, R20, C7 22u
Q1 IGBT_1 (R48)
Q2 IGBT_1 (R54)
R44, R46, R45, R43, C8 22u, R47
D3
R50, R52, R51, R49, C9 22u, R53
D4

U1 25C0108T
J1 CONN_12PIN (R4, R3)
R1, R2, C4 22u
Q3 IGBT_1 (R36)
Q4 IGBT_1 (R42)
R6, R8, R7, R5, C5 22u, R35
D1
R38, R40, R39, R37, C6 22u, R41
D2

U5 25C0108T
J4 CONN_12PIN (R26, R25)
R23, R24, C1 22u
Q5 IGBT_1 (R32)
Q6 IGBT_1 (R34)
R28, R30, R29, R27, C2 22u, R31
D17
R10, R12, R11, R9, C3 22u, R33
D9

U4 CASR50
J10 PINHEADER4
C13 22u, C14 22u, R71
Q10 IGBT_1
Q11 IGBT_1
R64

U3 25C0108T
J6 CONN_12PIN (R58, R57)
R55, R56, C10 22u
R60, R62, R61, R59, C11 22u, R63
D5
R66, R68, R67, R65, C12 22u, R69
D6
R70

COMPANY:	<Company Name>
TITLE:	<Title>
DRAWN: <Drawn By>	DATED: <Drawn Date>
CHECKED: <Checked By>	DATED: <Checked Date>
QUALITY CONTROL: <QC By>	DATED: <QC Date>
RELEASED: <Released By>	DATED: <Release Date>
CODE: <Code>	SIZE: D
DRAWING NO: <Drawing Number>	REV: <Revision>
SCALE: <Scale>	SHEET: 1 OF 1

Appendix B - Layout

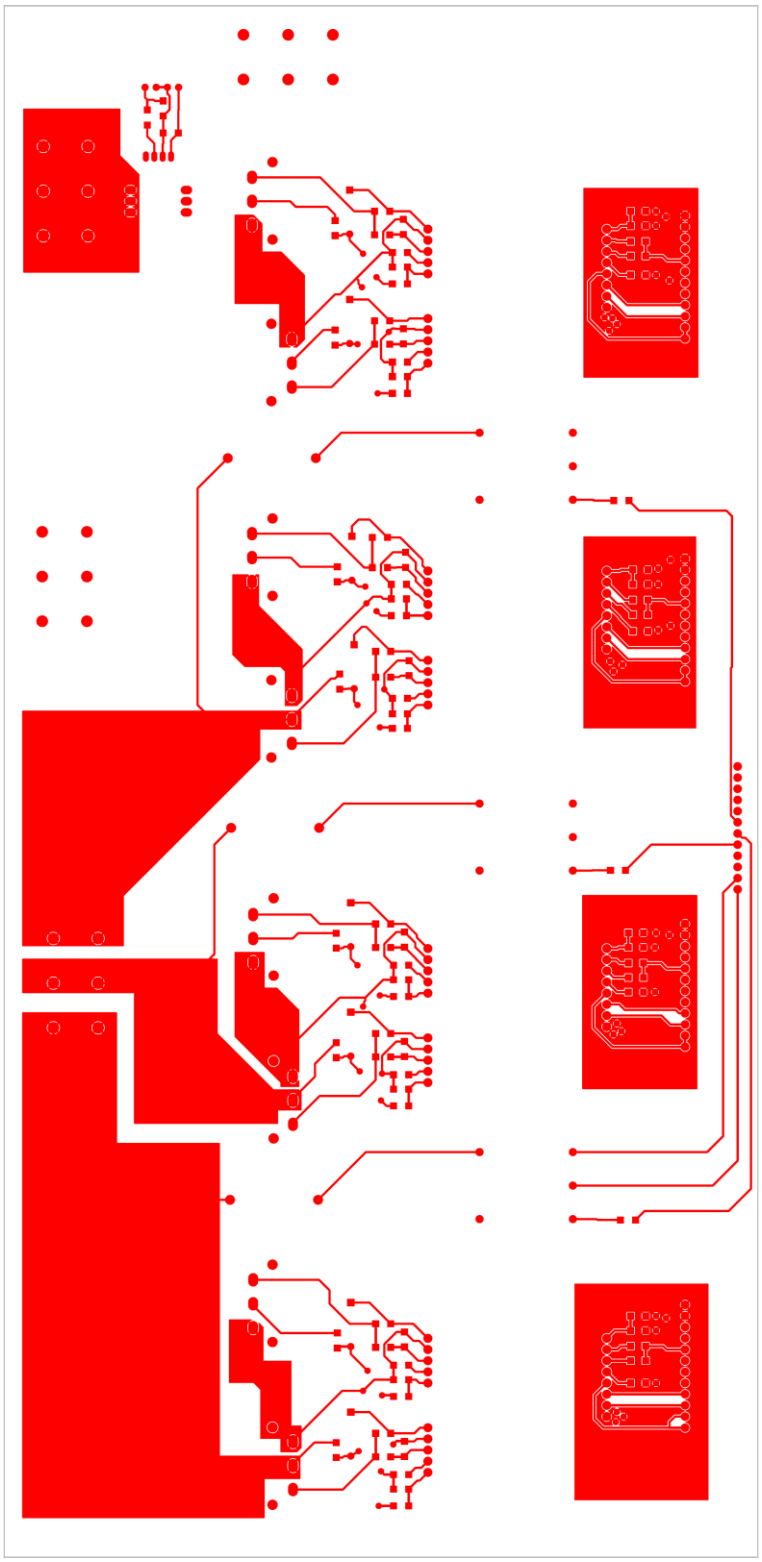

Figure 40: Top Layer

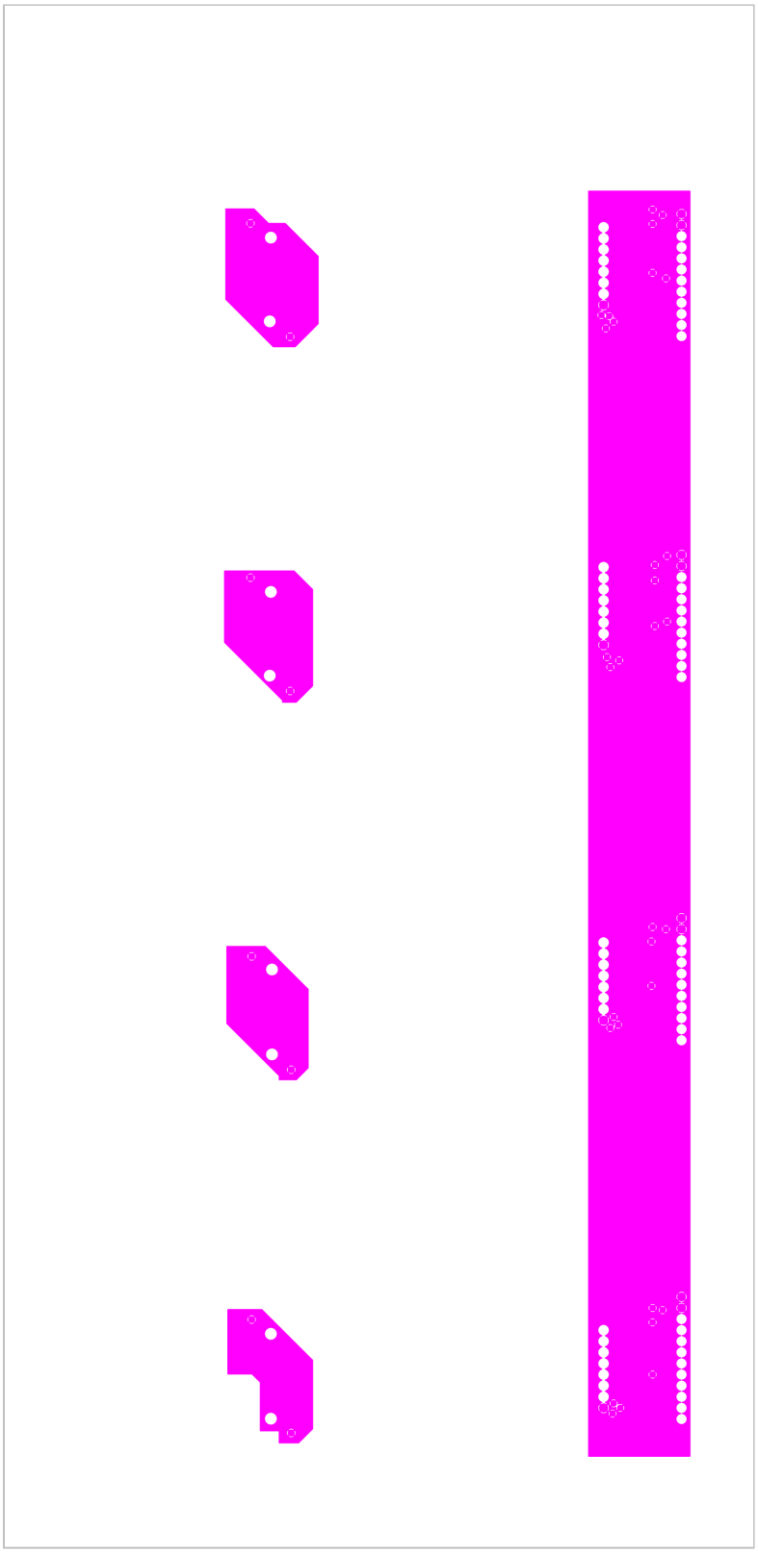

Figure 41: Layer 2

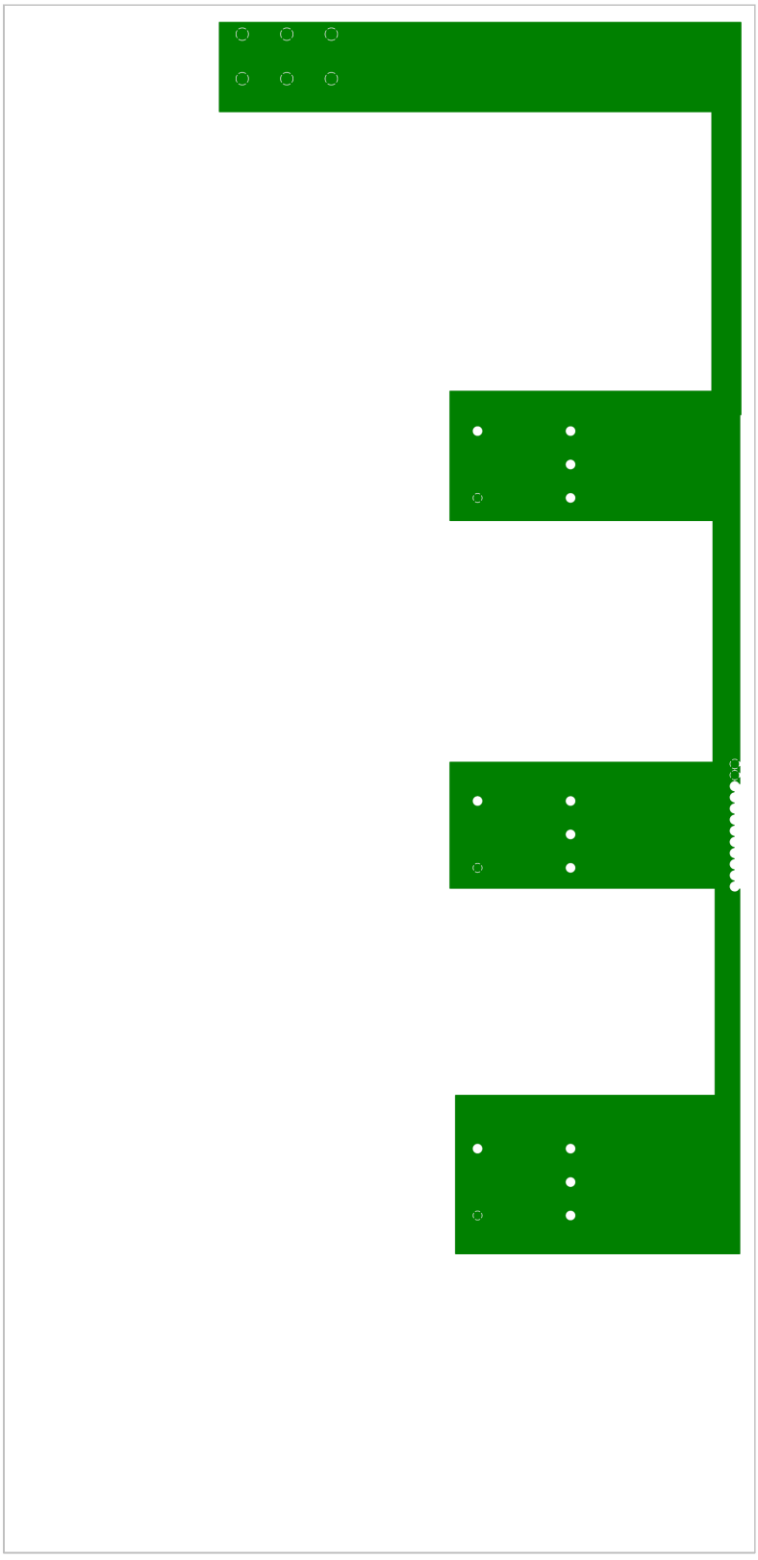

Figure 42: Layer 3

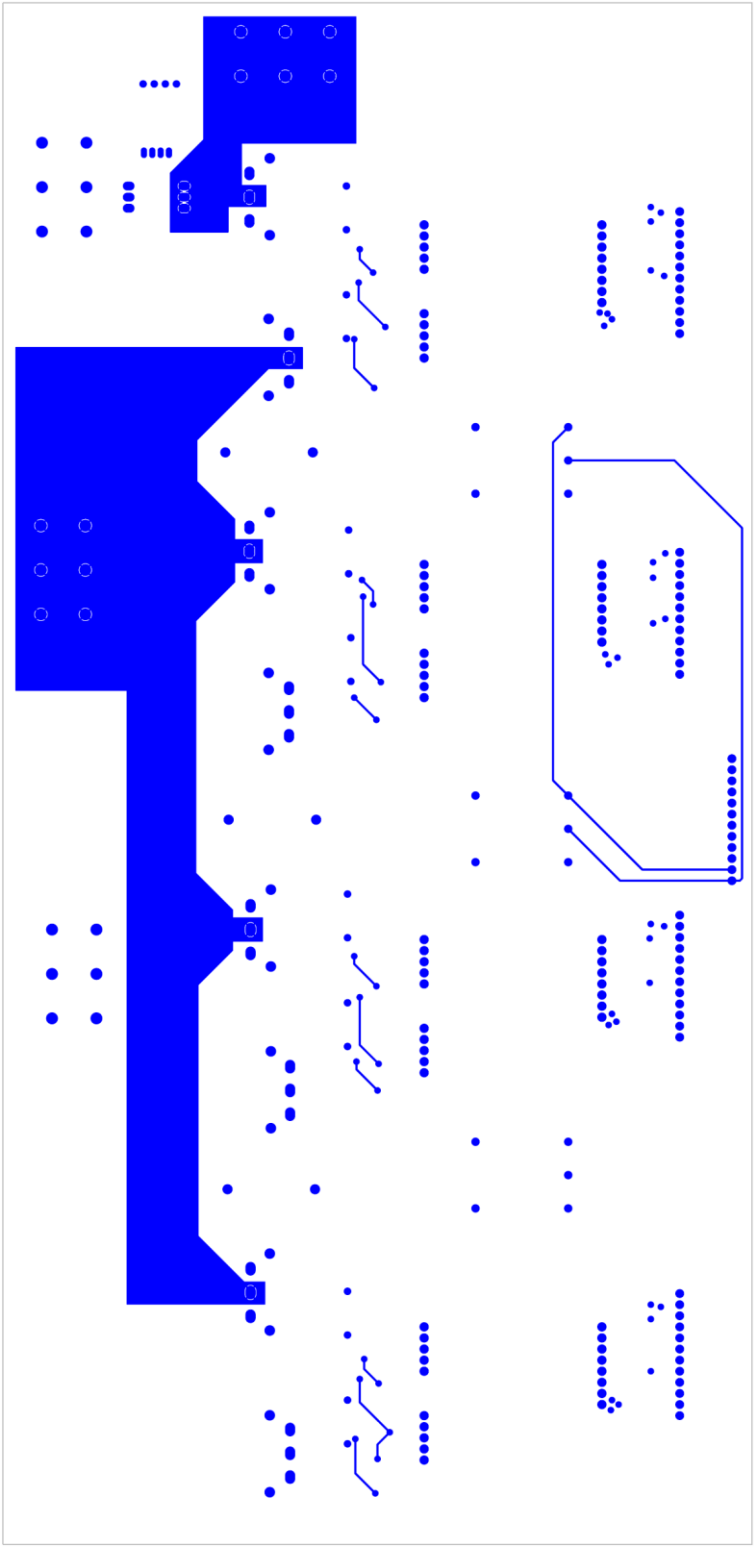

Figure 43: Bottom layer

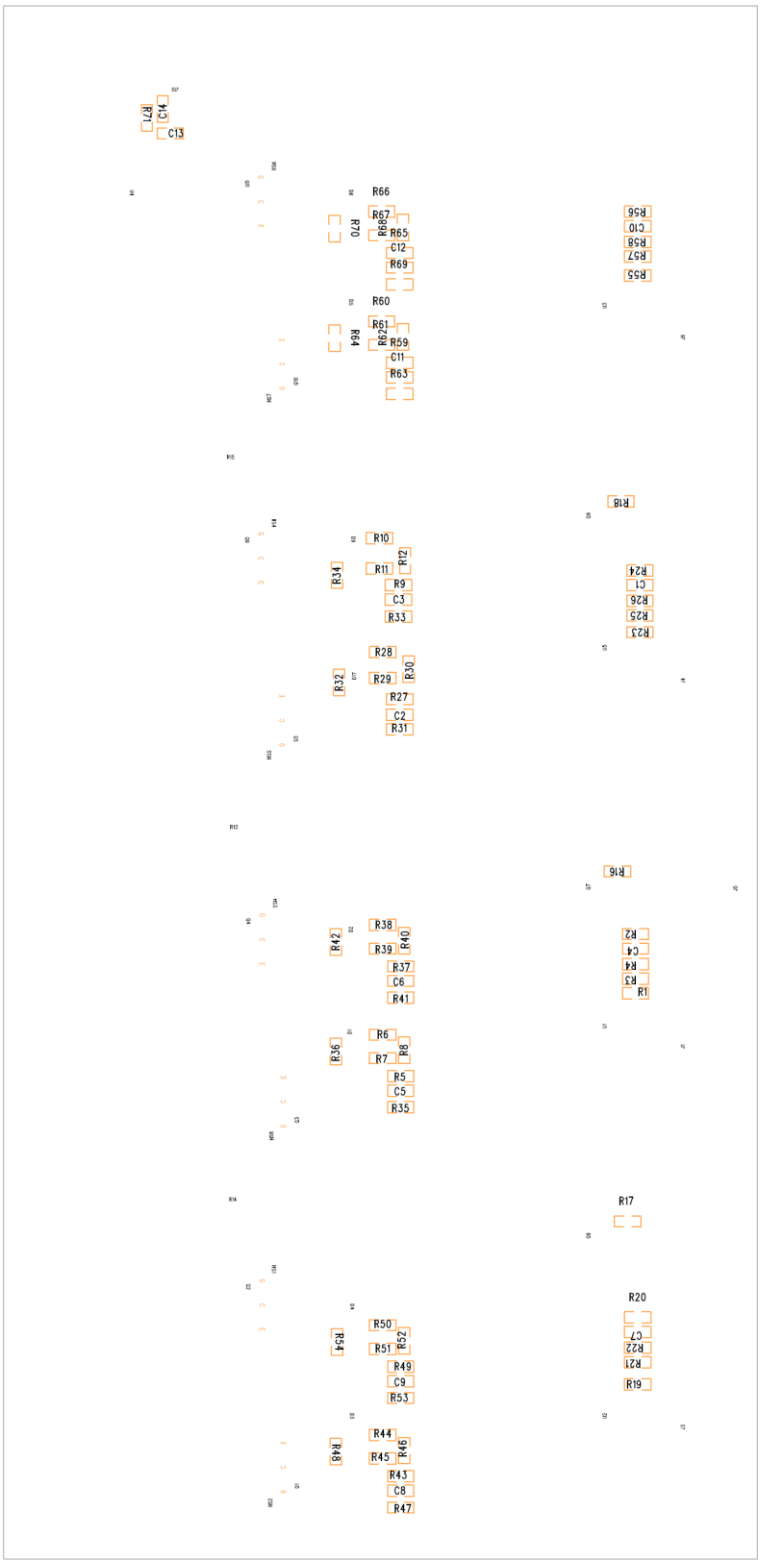

Figure 44: Locator

Appendix C – Power Supply Testing

The Functional testing of the power supply is described in tables below (Crandall 1997)

AC Input Tests:

Test name	Test Description
First Power-up	Apply 1.0 V to look for hard shorts, then proceed to 10 V input to look for shorts or excessive current conditions
Inrush Current	Discharge all capacitors. Apply maximum load. Apply AC voltage at the specified voltage, frequency and phase angle. Record the current drawn during the start-up
Softstart	Verify that the soft-start circuit is operational
High/Low line	Apply input at the maximum and minimum applicable voltage
Static Line Regulation	Output is allowed to stabilize after each transient. Apply pre-specified input voltages using the same step
Dynamic Line Regulation	Verify the output line regulation when the input voltage is changing.
Power Factor	PF measurement to verify the specified PF
Start-Up Time	Apply input voltage. Measure the time that all outputs are at the desired levels
Hold-Up Time	The time that the power supply holds the output at specified level after the input has been shut down

Leakage Current	This test is done at specified voltage. Both AC and DC currents are measured to ensure that there are no health risks due to too large leakage current
Grounding Tests	All ground potentials are measured. They shall exhibit some specified resistance to ensure the grounding is correct.
Ground Current	Measure the current from ground pin of the power cord from the power supply
Common Grounds	Resistance test between different ground potentials.
Isolated Ground	May be performed during HIPOT. In multiple output supplies, this test verifies that the grounds are not tied together
Specification requirement tests	Other tests may be tested according to the specifications that apply

DC Input Tests (Tests that are substantially different than in AC input tests):

Test name	Test Description
Inrush Current	Only the instantaneous current draw is measured.
Efficiency	Efficiency of the power supply shall be measured

AC Output Tests:

Test name	Test Description
Frequency Stability	To verify the stability of the output frequency.

Waveform Distortion	Waveform distortions when changes occur at the load current, reactive loads or loads with non-sinusoidal waveform are measured.
Spectral Purity	Measurement of the harmonic content of the output waveform
Current Limit	For verifying the different current limits.

DC Output Tests:

Test name	Test Description
Static Load Regulation	Output is stabilized in prior of measurement. Output is tested under various output currents and nominal input voltage
Dynamic Load Regulation	This test verifies the supply ability to maintain the output voltage under different load currents. The transient of the behavior is measured. Input will slew from 20 % to 80 % at 5A/µs
Short-Term Drift	Voltage drift. Checked during the prototype testing
Long-Term Drift	Voltage drift. Checked during the prototype testing
Thermal Drift	The power supply is usually checked for output voltage under different thermal stresses. Prototyping test
Ripple and Noise	Measured against the specification of the desired operation.
Overvoltage	To test the output short circuit event.
Isolation	Isolation of the AC/DC, noise currents and EMI/RFI. Verify against the applicable standard

DC and AC	HIPOT test or leakage test.
Noise and EMI	Accredited test laboratory is performing the EMI tests.
Sequencing	Testing the start-up or shut-down sequences.
Cross-Regulation	The percentage of voltage change in an output caused by a change of a different source
Current Limit and Short-circuit protection	Use the fixed resistor, adjustable or electronic load at the output to verify the features.

Control Inputs:

Test name	Test Description
Power Enable/Disable	This test verifies that the input of the power supply enable/disable control is working.
Master Clock Input	Some supplies have clock input to control the EMI/RFI. Also the lost signal case is tested

Ancillary Outputs:

Test name	Test Description
AC OK	The time that OK signal will operate after the input has reached the specified voltage that it should trigger the OK signal
DC OK	The time that OK signal will operate after the input has reached the specified voltage that it should trigger the OK signal
Remote Control Bus Interface	Tests any bus included in the power supply. Testing according the bus standard.

Master/Slave Clock Sync Circuits	Testing the master/slave sync I/O ports. Measurement of the specified output signals.

Appendix D - IGBT

IHW40N120R3

Resonant Switching Series

Reverse conducting IGBT with monolithic body diode

Features:

- Powerful monolithic body diode with low forward voltage designed for soft commutation only
- TRENCHSTOP™ technology offering:
- very tight parameter distribution
- high ruggedness, temperature stable behavior
- low V_{CEsat}
- easy parallel switching capability due to positive temperature coefficient in V_{CEsat}
- Low EMI
- Qualified according to JESD-022 for target applications
- Pb-free lead plating; RoHS compliant
- Halogen free (according to IEC 61249-2-21)
- Complete product spectrum and PSpice Models: http://www.infineon.com/igbt/

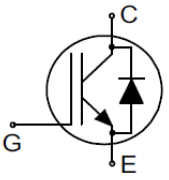

Applications:

- Inductive cooking
- Inverterized microwave ovens
- Resonant converters
- Soft switching applications

Package pin definition:

- Pin 1 - gate
- Pin 2 & backside - collector
- Pin 3 - emitter

Green

Halogen-Free

RoHS

Key Performance and Package Parameters

Type	V_{CE}	I_C	V_{CEsat}, T_{vj}=25°C	T_{vjmax}	Marking	Package
IHW40N120R3	1200V	40A	1.55V	175°C	H40R1203	PG-TO247-3

Maximum Ratings

For optimum lifetime and reliability, Infineon recommends operating conditions that do not exceed 80% of the maximum ratings stated in this datasheet.

Parameter	Symbol	Value	Unit
Collector-emitter voltage	V_{CE}	1200	V
DC collector current, limited by T_{vjmax} T_C = 25°C T_C = 100°C	I_C	 80.0 40.0	A
Pulsed collector current, t_p limited by T_{vjmax}	I_{Cpuls}	120.0	A
Turn off safe operating area $V_{CE} \le 1200V$, $T_{vj} \le 175°C$	-	120.0	A
Diode forward current, limited by T_{vjmax} T_C = 25°C T_C = 100°C	I_F	 80.0 40.0	A
Diode pulsed current, t_p limited by T_{vjmax}	I_{Fpuls}	120.0	A
Gate-emitter voltage Transient Gate-emitter voltage ($t_p \le 10\mu s$, D < 0.010)	V_{GE}	±20 ±25	V
Power dissipation T_C = 25°C Power dissipation T_C = 100°C	P_{tot}	429.0 215.0	W
Operating junction temperature	T_{vj}	-40...+175	°C
Storage temperature	T_{stg}	-55...+175	°C
Soldering temperature, wave soldering 1.6mm (0.063in.) from case for 10s		260	°C
Mounting torque, M3 screw Maximum of mounting processes: 3	M	0.6	Nm

Thermal Resistance

Parameter	Symbol	Conditions	Max. Value	Unit
Characteristic				
IGBT thermal resistance, junction - case	$R_{th(j-c)}$		0.35	K/W
Diode thermal resistance, junction - case	$R_{th(j-c)}$		0.35	K/W
Thermal resistance junction - ambient	$R_{th(j-a)}$		40	K/W

Electrical Characteristic, at T_{vj} = 25°C, unless otherwise specified

Parameter	Symbol	Conditions	Value			Unit
			min.	typ.	max.	
Static Characteristic						
Collector-emitter breakdown voltage	$V_{(BR)CES}$	V_{GE} = 0V, I_C = 0.20mA	1200	-	-	V
Collector-emitter saturation voltage	V_{CEsat}	V_{GE} = 15.0V, I_C = 40.0A T_{vj} = 25°C T_{vj} = 125°C T_{vj} = 175°C	 - - -	 1.55 1.80 1.90	 1.75 - -	V
Diode forward voltage	V_F	V_{GE} = 0V, I_F = 40.0A T_{vj} = 25°C T_{vj} = 125°C T_{vj} = 175°C	 - - -	 1.60 1.70 1.80	 1.80 - -	V
Gate-emitter threshold voltage	$V_{GE(th)}$	I_C = 1.00mA, V_{CE} = V_{GE}	5.1	5.8	6.4	V
Zero gate voltage collector current	I_{CES}	V_{CE} = 1200V, V_{GE} = 0V T_{vj} = 25°C T_{vj} = 175°C	 - -	 - -	 100.0 2500.0	µA
Gate-emitter leakage current	I_{GES}	V_{CE} = 0V, V_{GE} = 20V	-	-	100	nA
Transconductance	g_{fs}	V_{CE} = 20V, I_C = 40.0A	-	35.3	-	S
Integrated gate resistor	r_G			none		Ω

Electrical Characteristic, at T_{vj} = 25°C, unless otherwise specified

Parameter	Symbol	Conditions	Value			Unit
			min.	typ.	max.	
Dynamic Characteristic						
Input capacitance	C_{ies}	V_{CE} = 25V, V_{GE} = 0V, f = 1MHz	-	2708	-	pF
Output capacitance	C_{oes}		-	87	-	
Reverse transfer capacitance	C_{res}		-	76	-	
Gate charge	Q_G	V_{CC} = 960V, I_C = 40.0A, V_{GE} = 15V	-	335.0	-	nC
Internal emitter inductance measured 5mm (0.197 in.) from case	L_E		-	13.0	-	nH

Switching Characteristic, Inductive Load

Parameter	Symbol	Conditions	Value			Unit
			min.	typ.	max.	
IGBT Characteristic, at T_{vj} = 25°C						
Turn-off delay time	$t_{d(off)}$	T_{vj} = 25°C, V_{CC} = 600V, I_C = 40.0A, V_{GE} = 0.0/15.0V, $R_{G(on)}$ = 7.5Ω, $R_{G(off)}$ = 7.5Ω, $L\sigma$ = 220nH, $C\sigma$ = 40pF $L\sigma$, $C\sigma$ from Fig. E Energy losses include "tail" and diode reverse recovery.	-	336	-	ns
Fall time	t_f		-	38	-	ns
Turn-off energy	E_{off}		-	2.02	-	mJ
Turn-off energy, soft switching	E_{off}	dv/dt = 150.0V/µs	-	0.48	-	mJ

Switching Characteristic, Inductive Load

Parameter	Symbol	Conditions	Value			Unit
			min.	typ.	max.	
IGBT Characteristic, at T_{vj} = 175°C						
Turn-off delay time	$t_{d(off)}$	T_{vj} = 175°C, V_{CC} = 600V, I_C = 40.0A, V_{GE} = 0.0/15.0V, $R_{G(on)}$ = 7.5Ω, $R_{G(off)}$ = 7.5Ω, Lσ = 220nH, Cσ = 40pF Lσ, Cσ from Fig. E Energy losses include “tail” and diode reverse recovery.	-	410	-	ns
Fall time	t_f		-	96	-	ns
Turn-off energy	E_{off}		-	3.93	-	mJ
Turn-off energy, soft switching	E_{off}	*dv/dt* = 150.0V/µs	-	0.78	-	mJ

Appendix E – IGBT Driver

power integrations

2SC0108T2A0-17 Preliminary Data Sheet

Dual Channel Ultra-compact Low-cost SCALE™-2 Driver Core

Short Description

The low-cost SCALE™-2 dual-driver core 2SC0108T2A0-17 combines unrivalled compactness with broad applicability. The driver is designed for universal applications requiring high reliability. The 2SC0108T2A0-17 drives all usual IGBT modules up to 600A/1200V or 450A/1700V. The embedded paralleling capability allows easy inverter design covering higher power ratings. Multi-level topologies are also supported.

The 2SC0108T2A0-17 is the most compact driver core available for industrial applications, with a footprint of only 45 x 34.3mm and an insertion height of max. 16mm. It allows even the most restricted insertion spaces to be efficiently used. Compared with conventional drivers, the highly integrated SCALE-2 chipset allows about 85% of components to be dispensed with. This advantage is impressively reflected in increased reliability at simultaneously minimized cost.

The 2SC0108T2A0-17 combines a complete two-channel driver core with all components required for driving, such as an isolated DC/DC converter, short-circuit protection as well as supply voltage monitoring. Each of the two output channels is electrically isolated from the primary side and the other secondary channel.

An output current of 8A and 1W drive power is available per channel, making the 2SC0108T2A0-17 an ideal driver platform for universal usage in small and medium power applications. The driver provides a gate voltage swing of +15V/–8V. The turn-on voltage is regulated to maintain a stable 15V regardless of the output power level.

Its outstanding EMC allows safe and reliable operation in even hard industrial applications.

Product Highlights

- ✓ Ultra-compact dual channel driver
- ✓ Highly integrated SCALE-2 chipset
- ✓ Gate current ±8A, 1W output power per channel
- ✓ +15V/-8V gate driving
- ✓ Blocking voltages up to 1700V
- ✓ Safe isolation to EN 50178
- ✓ Short delay and low jitter
- ✓ Interface for 3.3V...15V logic level
- ✓ UL recognition E321757 for UL508C (NMMS2/8)
- ✓ UL recognition E346491 for UL60950-1 (NWGQ2/8)

Applications

- ✓ General purpose drives
- ✓ Uninterruptible power supplies (UPS)
- ✓ Solar and wind power converters
- ✓ Auxiliary converters for traction
- ✓ Electro/hybrid drive vehicles
- ✓ Driving parallel-connected IGBTs
- ✓ Switched mode power supplies (SMPS)
- ✓ Medical (MRT, CT, X-Ray)
- ✓ Laser technology

Preliminary Data Sheet

Safety Notice!

The data contained in this data sheet is intended exclusively for technically trained staff. Handling all high-voltage equipment involves risk to life. Strict compliance with the respective safety regulations is mandatory!

Any handling of electronic devices is subject to the general specifications for protecting electrostatic-sensitive devices according to international standard IEC 60747-1, Chapter IX or European standard EN 100015 (i.e. the workplace, tools, etc. must comply with these standards). Otherwise, this product may be damaged.

Important Product Documentation

This data sheet contains only product-specific data. For a detailed description, must-read application notes and important information that apply to this product, please refer to "2SC0108T Description & Application Manual" on www.power.com/igbt-driver/go/2SC0108T

Absolute Maximum Ratings

Parameter	Remarks	Min	Max	Unit
Supply voltage V_{CC}	VCC to GND	0	16	V
Logic input and output voltages	Primary side, to GND	-0.5	VCC+0.5	V
SOx current	Failure condition, total current		20	mA
Gate peak current I_{out}	Note 1	-8	+8	A
External gate resistance	Turn-on and turn-off	2		Ω
IGBT gate charge			6.3	µC
Average supply current I_{CC}	Notes 2, 3		260	mA
Output power	Ambient temperature <70°C (Notes 4, 5)		1.2	W
	Ambient temperature <85°C (Note 4)		1	W
Test voltage (50Hz/1min.)	Primary to secondary (Note 14)		5000	$V_{AC(eff)}$
	Secondary to secondary (Note 14)		4000	$V_{AC(eff)}$
Switching frequency f			50	kHz
|dV/dt|	Rate of change of input to output voltage (Note 10)		75	kV/µs
Operating voltage	Primary/secondary, secondary/secondary		1700	V_{peak}
Operating temperature	Notes 5, 18	-20	+85	°C
Storage temperature		-40	+90	°C

Recommended Operating Conditions

Power Supply	Remarks	Min	Typ	Max	Unit
Supply voltage V_{CC}	VCC to GND	14.5	15	15.5	V

Electrical Characteristics

All data refer to +25°C and V_{CC} = 15V unless otherwise specified.

Power supply	**Remarks**	**Min**	**Typ**	**Max**	**Unit**
Supply current I_{CC}	Without load		31		mA
Coupling capacitance C_{io}	Primary side to secondary side, per channel		19		pF
Power Supply Monitoring	**Remarks**	**Min**	**Typ**	**Max**	**Unit**
Supply threshold V_{CC}	Primary side, clear fault	11.9	12.6	13.3	V
	Primary side, set fault (Note 11)	11.3	12.0	12.7	V
Monitoring hysteresis	Primary side, set/clear fault	0.35			V
Supply threshold V_{ISOx}-V_{Ex}	Secondary side, clear fault	12.1	12.6	13.1	V
	Secondary side, set fault (Note 12)	11.5	12.0	12.5	V
Monitoring hysteresis	Secondary side, set/clear fault	0.35			V
Supply threshold V_{Ex}-V_{COMx}	Secondary side, clear fault	5	5.15	5.3	V
	Secondary side, set fault (Note 12)	4.7	4.85	5	V
Monitoring hysteresis	Secondary side, set/clear fault	0.15			V
Logic Inputs and Outputs	**Remarks**	**Min**	**Typ**	**Max**	**Unit**
Input bias current	V(INx) > 3V		190		µA
Turn-on threshold	V(INx)		2.6		V
Turn-off threshold	V(INx)		1.3		V
SOx output voltage	Failure condition, I(SOx)<20mA			0.7	V
Short-Circuit Protection	**Remarks**	**Min**	**Typ**	**Max**	**Unit**
Current through pin REFx	R(REFx, VEx)<70kΩ		150		µA
Minimum response time	Note 8		1.2		µs
Minimum blocking time	Note 9		9		µs
Timing Characteristics	**Remarks**	**Min**	**Typ**	**Max**	**Unit**
Turn-on delay $t_{d(on)}$	Note 6		90		ns
Turn-off delay $t_{d(off)}$	Note 6		75		ns
Jitter of turn-on delay	Note 17		±2		ns
Jitter of turn-off delay	Note 17		±2		ns
Output rise time $t_{r(out)}$	Note 7		17		ns
Output fall time $t_{f(out)}$	Note 7		15		ns
Transmission delay of fault state	Note 13		360		ns

Electrical Isolation	Remarks	Min	Typ	Max	Unit
Test voltage (50Hz/1s)	Primary to secondary side (Note 14)	5000	5050	5100	V_{eff}
	Secondary to secondary side (Note 14)	4000	4050	4100	V_{eff}
Partial discharge extinction volt.	Primary to secondary side (Note 16)	1768			V_{peak}
	Secondary to secondary side (Note 16)	1700			V_{peak}
Creepage distance	Primary to secondary side	12.9			mm
	Secondary to secondary side	8.5			mm
Clearance distance	Primary to secondary side	12.9			mm
	Secondary to secondary side	6.5			mm

Outputs	Remarks	Min	Typ	Max	Unit
Blocking capacitance	VISOx to VEx		9.4		µF
	VEx to COMx		9.4		µF
Typical internal gate resistance	Turn-on and turn-off (Note 15)		0.5		Ω

Output voltage swing

The output voltage swing consists of two distinct segments. First, there is the turn-on voltage V_{GHx} between pins GHx and VEx. V_{GHx} is regulated and maintained at a constant level for all output power values and frequencies.
The second segment of the output voltage swing is the turn-off voltage V_{GLx}. V_{GLx} is measured between pins GLx and VEx. It is a negative voltage. It changes with the output power to accommodate the inevitable voltage drop across the internal DC/DC converter.

Output Voltage	Remarks	Min	Typ	Max	Unit
Turn-on voltage, V_{GHx}	Any load condition		15.0		V
Turn-off voltage, V_{GLx}	No load		-9.4		V
Turn-off voltage, V_{GLx}	1W output power		-7.6		V
Turn-off voltage, V_{GLx}	1.2W output power		-7.2		V

Appendix F – Litz Wire

Structure		External diameter without wrapping		External diameter with wrapping 1 x 52 (1 x Natural silk)		External diameter with wrapping 2 x 52 (2 x Natural silk)		Cross-section	DC-Resistance at 20°C (68°F)			Metres per kg
No. of strands	diameter of single wire [mm]	min [mm]	max [mm]	min [mm]	max [mm]	min [mm]	max [mm]	[mm²]	min [Ω/km]	nom [Ω/km]	max [Ω/km]	nom [m/kg]
	0.016 AWG 54	Other dimensions on request										
	0.020 AWG 52	Other dimensions on request										
	0.022 AWG 51	Other dimensions on request										
	0.025 AWG 50	Other dimensions on request										
10		0.127	0.142	0.157	0.177	0.187	0.212	0.00707	2176	2467	2713	11764
20		0.179	0.200	0.209	0.235	0.239	0.270	0.01414	1088	1233	1357	6060
25								0.01767				4964
30								0.02121				3921
35				External diameter depending on type of wrapping. Dimensions on request				0.02474				3355
45								0.03181				2611
60	0.03							0.04241				1960
75								0.05301				1567
90	AWG 48							0.06362				1307
105								0.07422				1119
120								0.08482				980
135								0.09542				871
180								0.12723				653
225								0.15904				522
270								0.19085				435
10		0.407	0.451	0.442	0.491	0.467	0.521	0.08011	205	222	235	1300
12		0.452	0.502	0.487	0.542	0.512	0.572	0.09613	170	185	196	1079
15		0.498	0.553	0.533	0.593	0.568	0.633	0.12017	136	148	157	803
20		0.574	0.638	0.609	0.678	0.644	0.718	0.16022	102	111	118	647
25		0.642	0.714	0.678	0.754	0.713	0.794	0.20028	82	89	94	518
30		0.704	0.782	0.739	0.822	0.774	0.862	0.24033	68	74	81	432
35		0.761	0.845	0.796	0.885	0.851	0.945	0.28039	58	63	69	370
45		0.862	0.957	0.897	0.997	0.952	1.057	0.36050	45.5	49.3	53.9	288
60		1.003	1.113	1.038	1.153	1.093	1.213	0.48066	34.1	37.0	41.2	203
75		1.123	1.246	1.158	1.286	1.213	1.346	0.60083	27.3	26.9	33.0	163
90		1.232	1.367	1.267	1.407	1.322	1.467	0.72100	22.7	24.7	27.5	136
105		1.330	1.476	1.365	1.516	1.420	1.576	0.84116	19.5	21.1	23.5	116
120		1.417	1.573	1.452	1.613	1.507	1.673	0.96133	17.0	18.5	20.6	102
135	0.10	1.504	1.670	1.539	1.710	1.594	1.770	1.08150	15.2	16.4	18.3	90
140			1.65					1.10	14.6	15.9	16.8	87
175	AWG 38		1.83	External diameter depending on type of wrapping. Dimensions on request				1.38	11.7	12.7	13.4	70
210			2.01					1.65	9.8	10.6	11.2	58
245			2.16					1.93	8.4	9.1	9.6	50
280			2.34					2.20	7.3	7.9	8.4	44
350			2.62					2.75	5.9	6.3	6.7	35
420			2.95					3.30	4.9	5.3	5.6	27
525			3.27					4.13	3.9	4.2	4.5	22
630			3.59					4.95	3.3	3.5	3.7	18
735			3.87					5.77	2.8	3.0	3.2	16
840			4.19					6.60	2.4	2.6	2.8	14
945			4.40					7.42	2.2	2.3	2.5	12
1050			4.68					8.25	1.9	2.1	2.2	11
1260			5.12					9.90	1.6	1.8	1.9	9
1400			5.49					10.99	1.5	1.6	1.7	8

PACK
Feindrähte

Rudolf Pack GmbH & Co.
Am Bäuweg 9-11
D-51645 Gummersbach

Tel.: +49|0) 22 61/95 67- 0
Fax: +49|0) 22 61/95 67-67

www.pack-feindraehte.de
info@pack-feindraehte.de

Technical Data

RUPALIT® Litz wire

(The technical data comply in part with the specification given in standard IEC 60317-11)

RUPALIT® high-frequency litz wires are constructed from enamelled copper wire (magnet wire) made of RUPOL®, RUPEX® or RUTHERM® – see illustrations below. (Aluminium magnet wires on request)